J. Fluid Mech. (2014), *vol.* 742, *pp* 577–617. © Cambridge University Press 2014
doi:10.1017/jfm.2014.15

Growth of multiparticle aggregates in sedimenting suspensions

Alexander Z. Zinchenko† and Robert H. Davis

Department of Chemical and Biological Engineering, University of Colorado, Boulder, CO 80309-0424, USA

(Received 25 July 2013; revised 18 November 2013; accepted 31 December 2013; first published online 24 February 2014)

The process of multiparticle aggregation in a dilute sedimenting suspension is rigorously simulated, with precise hydrodynamical interactions. The primary particles are monodisperse non-Brownian spheres at zero Reynolds number, with short-range molecular attractions. The rigid aggregates grow, as they settle downwards, by sequential particle addition – a valid assumption for dilute suspensions during the initial stages. The growth starts from doublet–particle interaction, but the indeterminate initial doublet concentration does not affect the results for cluster geometry and settling velocity. A new particle is generated far below a cluster with uniform probability density, and many trial particle–cluster relative trajectories are computed with high accuracy until a collision is found. The new cluster is then assumed to be rigid and allowed to reach a steady sedimentation regime (which is a spiral motion around the axis of steady rotation, ASR) before another particle is added, and so on. The ASR is typically far away from the cluster centre of mass. The Stokes flow solution algorithm for particle–cluster interaction works very efficiently with high-order multipoles (to order 100) and is extended to arbitrarily small particle–cluster separations by a geometry perturbation adapted from the conductivity simulations of Zinchenko (*Phil. Trans. R. Soc. Lond.* A, 1998, vol. 356, pp. 2953–2998). Clusters are generated to $N = 100$ spheres, with extensive averaging over many growth realizations. The fractal scaling $\sim N^{0.48}$ for the cluster settling speed is quickly attained once $N \geqslant 25$, and the exponent 0.48 is practically independent of the strength of molecular forces. The cluster fractal dimension is predicted to be $d_f = 1.91 \pm 0.02$ (in contrast to the existing views that sequential addition can only produce high-d_f clusters). Several average characteristics of the cluster size are also computed. The theoretical settling speed has no adjustable parameters and agrees reasonably well with prior experiments for a moderately polydisperse system in a broad range of cluster sizes.

Key words: suspensions, particle/fluid flow, fractals

1. Introduction

Flocculation of suspended small particles into large aggregates is a common phenomenon related to many processes in bioreactors, differential settlers and natural marine systems. The main growth mechanisms include Brownian, flow-induced and

† Email address for correspondence: alexander.zinchenko@colorado.edu

https://doi.org/10.1017/jfm.2014.15 Published online by Cambridge University Press

gravitational coagulation. Being able to predict the settling speed of multiparticle clusters formed in differential sedimentation is important, e.g. for water treatment processes. So far, all computer simulations of settling behaviour, though, have assumed that a rigid cluster is first generated by a version of the Monte Carlo (MC) method, typically in the limits of diffusion-limited (DLCA) or reaction-limited (RLCA) cluster–cluster aggregation. In these schemes, already existing clusters are moved randomly (without any interactions) to meet and form larger clusters with some sticking probability (from unity for DLCA, to near-zero for RLCA). These algorithms produce open clusters with the fractal dimension (the exponent d_f in the scaling $M \sim R^{d_f}$ between the average cluster mass M and radius R) in the range 1.78–2.2 (see Meakin 1984; Jullien, Botet & Mors 1987; Meakin & Family 1987, and references therein). More recent tunable-dimension algorithms (Thouy & Jullien 1996; Ehrl, Soos & Lattuada 2009) produce clusters with any given d_f from 1 to 3. The library of clusters built in this manner is then used to simulate the orientationally and ensemble-averaged hydrodynamical drag force and hence the settling speed by Lattice Boltzmann (LB; Binder *et al.* 2006; Chopard, Nguyen & Stoll 2006), (accelerated) Stokesian Dynamics ((A)SD; Binder *et al.* 2006; Harshe, Ehrl & Lattuada 2010) or rigorous multipole (Filippov 2000) methods. Binder, Hartig & Peukert (2009) added a realistic feature to the work of Binder *et al.* (2006), allowing their DLCA clusters to reorient during sedimentation and reach a steady settling speed. For these particular applications, periodic boundary conditions in LB and ASD create an undesirable strong artificial effect of the box size on the settling behaviour. To extract a single-cluster settling speed from LB simulations, it was possible (Chopard *et al.* 2006) to first find a two-parameter rescaling fit to the analytical solution of Sangani & Acrivos (1982) for a small sphere settling in a periodic box. Such a procedure, though, requires much data from LB and would not be practicable in dynamical simulations (of primary interest in the present work). To avoid similar difficulties, Binder *et al.* (2009) dynamically calculated the steady-state cluster orientation in a small box only, and then used this orientation in a static, but still costly, ASD simulation for a large box.

Note that all the above cluster generation methods have *ad hoc* features and are recognized (Lattuada, Wu & Morbidelli 2003) as oversimplifications even in the Brownian regime. They also do not address relevant physics of the cluster growth mechanism in sedimenting suspensions of non-Brownian particles, in which cluster formation and sedimentation are coupled. Tunable dimension algorithms (see above) add even more uncertainty by making d_f a truly free parameter set at will. It would be more instructive to instead generate clusters from a physically well-defined growth mechanism with rigorous mathematical modelling, and thereby predict d_f (among many other average aggregate properties).

The present work addresses this issue, for the first time, for dilute sedimenting suspensions of monodisperse non-Brownian spheres. The principal assumption is that aggregates grow, as they settle, by sequential particle addition, one at a time. Following Sutherland (1966), it is widely stated (e.g. Vanni 2000, and references therein) that growth models with sequential addition can only produce high fractal dimensions $d_f = 2.5$–3.0 (rarely observed in experiments), as opposed to cluster–cluster aggregation (CCA) giving open clusters with smaller d_f. A common underlying argument is that single additional particles can reach the cluster core, thus promoting the development of dense, high-d_f clusters (while, in contrast, large added aggregates have to stay on the periphery). This argument is flawed for non-Brownian particle systems, though, owing to hydrodynamical interactions. Indeed, for a single particle

https://doi.org/10.1017/jfm.2014.15 Published online by Cambridge University Press

approaching a cluster from large distances, the cluster (despite its complex, fractal-like shape) acts as a sphere of a large hydrodynamical radius, effectively preventing the primary particle from reaching the cluster core. Instead, the particle is often swept around the cluster and tends to be captured near the periphery, if at all. Our counter-argument is well supported by the present calculations giving realistic results that are in good agreement with experiments. The validity of the sequential addition scheme, though, is limited to the initial aggregation stages, while the primary particle concentration is still not far from its initial value (which does not preclude large clusters from forming). A study of the model form of the population dynamics equations for flow-induced aggregation (Torres, Russel & Schowalter 1991*a*,*b*) suggests that CCA becomes, indeed, a dominant growth mechanism at later stages. Unfortunately, at present, we do not see a realistic way to include CCA in rigorous cluster growth simulations. We only note a substantial difference between the gravity-induced and flow-induced aggregation processes: in the former, the ability of two clusters to aggregate is greatly reduced when they are of similar size, due to comparable settling speeds. Presumably, this feature can extend the range of validity of the sequential addition scheme in differential settling, compared to flow-induced aggregation.

The plan of this paper is as follows. The problem formulation and the general solution scheme are outlined in § 2. Short-range molecular attractions are included to overcome lubrication and provide for ultimate particle–cluster contact at collisions. In § 3, new semi-analytical tools are described to approach and characterize the steady sedimentation regime after a particle attaches to an aggregate. These simple tools greatly benefit from free-space boundary conditions and are far more efficient than numerical integration for cluster orientation in a periodic box. A realistic yet efficient scheme for generating new particle positions away from the cluster (prior to trajectory integration) is non-trivial due to cluster rotation and fractal-like shape. This scheme, detailed in § 4, is substantially based on the analytical description of the steady-state regime for a single cluster from § 3. In § 5, we describe the rigorous Stokes flow multipole solution techniques for a rigid cluster interacting with a particle. These techniques, much different from simpler general schemes available in the literature for particle interactions, work very efficiently with high-order multipoles through rotational transformations, economical truncation of expansions/re-expansions and iterative solutions. The groundwork for these tools was laid in our previous multibody solutions (Zinchenko 1994; Zinchenko & Davis 2000; Zinchenko, Rother & Davis 2011). In addition, the idea of geometry perturbation (adapted from the conductivity simulations of Zinchenko (1998)) helps to resolve lubrication and extends the algorithm to arbitrarily small particle–cluster separations. It would be interesting to compare our geometry perturbation method with a different general approach of Sangani & Mo (1994) to including lubrication in multipole solutions, but this task is beyond the scope of the present paper. Unlike ours, their approach uses a detailed form of the lubrication solution in the gap, and a cutoff angle (found by tuning) to define the lubrication area. Another recent approach to including lubrication, which is closer to that of Sangani & Mo (1994) than to ours, is the traction-corrected method of Ingber *et al.* (2008). Miscellaneous details of our cluster growth algorithm are given in § 6. In § 7, devoted to testing, a comprehensive comparison is made with high-resolution boundary-integral calculations for a small random particle–cluster configuration in near-contact to validate the present code. Dynamical simulation tests also validate the geometry perturbation scheme and high accuracy of particle–cluster trajectory calculation to collision, for both small and larger systems. In addition, we stress the importance of high-order multipoles for accurate trajectory analysis, even

https://doi.org/10.1017/jfm.2014.15 Published online by Cambridge University Press

with lubrication explicitly included. In § 8, the algorithm is systematically used for calculating average hydrodynamical and geometrical properties of clusters formed in differential settling. Our results are limited to $N \leqslant 100$ spheres, because extensive ensemble averaging is far more important here than generating a few clusters of a larger size. Still, three sets of 80 growth realizations for three levels of van der Waals attraction required a total of $\sim 10^6$ particle–cluster relative trajectories to be computed. The average quantities of interest here are the cluster settling speed versus N and its fractal scaling at $N \gg 1$ (related to d_f), different characteristics of the cluster size (hydrodynamical, gyration, outer radius, etc.) and the particle connectivity in a cluster. In § 9, comparisons are made with experiments. Conclusions are formulated in § 10.

2. Problem formulation and the general solution scheme

Consider the process of multiparticle aggregation in a dilute sedimenting monodisperse suspension. All suspended primary particles are solid spheres of the same radius a and uniform density ρ' sedimenting downwards in a quiescent Newtonian liquid of density $\rho < \rho'$ and viscosity μ. The particle size is small enough for the Stokes flow approximation to apply, but is also large enough to neglect Brownian motion:

$$\frac{U^S a\rho}{\mu} \ll 1, \quad \frac{a^4 \Delta\rho g}{kT} \gg 1, \quad U^S = \frac{2}{9}\frac{\Delta\rho g a^2}{\mu}. \tag{2.1}$$

Here, U^S is the settling speed of an isolated sphere, $\Delta\rho = \rho' - \rho$, g is the gravitational acceleration and kT is the Boltzmann temperature. Before the aggregation process, the suspension is random and homogeneous, with a uniform particle volume fraction $c \ll 1$ throughout. In the Stokes regime, two isolated equal spheres are known to sediment without changing their relative position and orientation, so the aggregation process cannot start unless a small difference in sizes, the effect of a third particle, non-Newtonian/inertial effects and/or possibly some other weak mechanisms are taken into account. To avoid these difficulties, we assume that some rigid two-particle aggregates of touching spheres are already present, with the volume fraction much smaller than c for primary particles. Neither of these quantities affects the results obtained in this work for the fractal geometry and sedimentation speed of clusters; kinetics of cluster growth is not considered herein. Such an aggregate, in its downward motion, captures the third primary particle to form a rigid triplet (figure 1). Doublet–doublet interactions are much less frequent and are neglected. Unless otherwise stated, the initial vertical doublet configuration, far away from the particle (figure 1*a*), is assumed in all our simulations. Such an initial condition is a strongly favoured choice; indeed, even a small difference in the particle sizes or densities in the doublet would eventually lead to vertical alignment. A limited comparison between the two types of simulation (with vertical alignment versus random initial doublet orientation) is made in § 8. For the third particle in figure 1(*a*), the initial horizontal position is chosen randomly with uniform probability density, as required for a homogeneous suspension. Generally, a large number of particle–doublet relative trajectories for different initial conditions have to be discarded, until the first trajectory leading to collision is found. The ultimate contact between the doublet and the particle in a finite time requires a singular van der Waals attractive force to overcome lubrication. In our calculations, this force (see below) is chosen to be short-range, i.e. small compared to the effective gravitational force $F^S = (4/3)\pi a^3 \Delta\rho g$ on a primary particle, except for near-contact. Once a three-particle aggregate is formed (figure 1*b*), it is assumed to be rigid but allowed

https://doi.org/10.1017/jfm.2014.15 Published online by Cambridge University Press

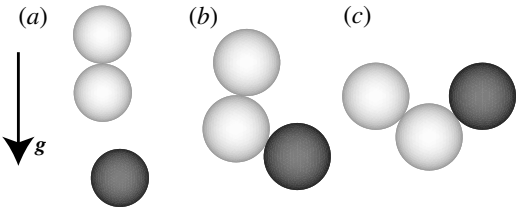


FIGURE 1. The initial stage of aggregate growth: (*a*) a vertically aligned doublet starts interacting with a new primary particle (dark shaded) randomly generated far below; (*b*) collision of the primary particle with the doublet to form a rigid triplet; (*c*) subsequent steady-state sedimentation of the triplet.

to rotate until the steady sedimentation regime is reached. For the triplet, this regime is simply vertical sedimentation without rotation in an isosceles configuration, the gravity vector $\boldsymbol{g}$ being in the plane of the particle centres and perpendicular to the triangle base (figure 1*c*). In general, once we have a rigid aggregate of $N \geqslant 3$ particles in a steady sedimentation regime, a new particle is randomly generated far below the aggregate with uniform probability density, and the particle–aggregate relative trajectory is computed. If no capture with the aggregate occurs, a new random initial particle location is tested, and so on, until a colliding trajectory is found. The new rigid-body aggregate with $N + 1$ particles is then allowed to reach the steady sedimentation regime (which is not a simple downward translation, but a spiral motion) before a new particle is generated. Our algorithm, therefore, rigorously simulates the process of aggregate growth in dilute sedimenting suspensions.

Technically, the algorithm consists of several parts:

A. An efficient, highly accurate multipole solution technique for the Stokes problem for a primary particle interacting with a rigid aggregate (often called 'cluster' or 'floc' in what follows) of N other particles. This technique includes lubrication and is suitable for dynamical simulations of many trajectories to near-contact.
B. Related, an efficient, highly accurate Stokes flow solution for an isolated rigid-body cluster of N spheres; just a simplification of part A.
C. Determining the regime of steady sedimentation for a cluster of N spheres.
D. A special strategy for generating random initial positions for a new primary particle, far below a cluster. This issue is non-trivial owing to steady cluster rotation and fractal-like cluster shapes.

Below, parts C and D are discussed first. More technical discussion of the multipole solutions A and B is delayed until § 5.

Note that, even with the best $O(N)$ implementations for the multiparticle solutions A and B, the overall computational effort to reach a cluster size of N cannot be less than $O(N^2)$, since the process should go through all intermediate stages with $N - 1$, $N - 2$, ... particles (unlike in the simplistic Monte Carlo algorithms for aggregate growth). Moreover, the average number of discarded particle–cluster trajectories (i.e. not leading to collisions) tends to grow slightly with N (§ 4), presumably due to more complex, fractal-like cluster shapes and relatively weaker van der Waals forces as N increases, so the actual scaling is slightly worse than $O(N^2)$. A very large total number of necessary trajectories is one reason why the present results are limited to $N \leqslant 100$. Another reason is that ensemble averaging over many process realizations (80) for systems of moderate size $N \leqslant 100$ was found to be far more important than generating

https://doi.org/10.1017/jfm.2014.15 Published online by Cambridge University Press

a few clusters of larger size. Finally, for larger clusters (which sediment faster), the role of inertial effects would increase; so would the role of hydrodynamical stresses capable of breaking rigid bonds between cluster particles.

Van der Waals attraction. For the potential of molecular attraction between two spheres with surface clearance εa, the simplest unretarded form is used (e.g. Verwey & Overbeek 1948)

$$\Phi = -\frac{A_H}{6}\left\{\frac{2}{s^2-4}+\frac{2}{s^2}+\ln\left(\frac{s^2-4}{s^2}\right)\right\}, \quad s = 2+\varepsilon, \tag{2.2}$$

where A_H is the Hamaker constant for the particle–fluid combination; the van der Waals attractive force is $\Phi'(s)/a$. Instead of the non-dimensional Hamaker parameter $A = A_H/(a^4\Delta\rho g)$, we prefer to characterize the relative strength of molecular attraction by the non-dimensional clearance ε_{vdW} at which the van der Waals force $\Phi'(s)/a$ equals the effective gravitational force F^S on a primary particle. Three values of $\varepsilon_{vdW} = 0.02$, 0.005 and 0.00125 ('strong', 'moderate' and 'weak' attraction, respectively) are considered; the corresponding values of A are 2.09×10^{-2}, 1.27×10^{-3} and 7.87×10^{-5}, respectively. Obviously, the assumption of rigidity of our multiparticle clusters is most realistic when singular van der Waals attraction is not mitigated by electrostatic repulsion.

On the validity of the sequential addition scheme. It is generally expected that our assumption of cluster growth through sequential addition (SA) of new particles, one at a time, is valid for dilute suspensions as long as the singlet concentration remains close to its initial value. For quantitative assessment, we numerically integrated the model forms of the spatially homogenous population dynamics equations for the number concentrations $N_i(t)$ of flocs containing $i \leqslant 50$ particles, for both CCA and SA growth models. The two sets of equations are given by (3.1) and (3.6), respectively, in Torres *et al.* (1991*b*). The collision rate between i- and j-particle flocs was modified from their $(R_i+R_j)^3$ (pertinent to flow-induced aggregation) to $(R_i+R_j)^2|R_j^2-R_i^2|$ for aggregation due to differential settling. The cluster capture radius varies as $R_i \sim i^{0.52}$, as follows from our results in § 8. The initial doublet concentration was $N_2 = 0.005N_1$. Even when N_1 is depleted to 85 % of its initial value, the differences between N_i from CCA and SA models stay within 20 % for all $i \leqslant 50$; the agreement is much better at smaller times.

3. Sedimentation of isolated multiparticle aggregates

Owing to the uniform density of primary particles, the gravitational forces are applied at the particle centres, so the balance equations for the total hydrodynamical force $\boldsymbol{F}_h$ and torque $\boldsymbol{T}_h$ acting on an aggregate are

$$\boldsymbol{F}_h + F^S N\boldsymbol{g}/g = \boldsymbol{0}, \quad \boldsymbol{T}_h = \boldsymbol{0}, \tag{3.1}$$

where N is the number of particles in the aggregate ('cluster mass', in what follows), and the torque $\boldsymbol{T}_h$ is calculated about the aggregate centre of mass $\boldsymbol{O}_g$. Owing to the linearity of the Stokes flow problem, predicting the temporal dynamics of the aggregate at $t>0$ only requires three Stokes flow solutions in the initial configuration $t=0$ (when a new primary particle is attached). Indeed, under the torque-free condition, for $t>0$ the centre-of-mass velocity $\boldsymbol{V}(t)$ and the aggregate rotational velocity $\boldsymbol{\Omega}(t)$ can be written in terms of the mobility tensors $\boldsymbol{M}_{\boldsymbol{VF}}$ and $\boldsymbol{M}_{\boldsymbol{\Omega F}}$:

$$\boldsymbol{V}(t) = -\boldsymbol{M}_{\boldsymbol{VF}}\boldsymbol{F}_h, \quad \boldsymbol{\Omega}(t) = \boldsymbol{M}_{\boldsymbol{\Omega F}}\boldsymbol{F}_h. \tag{3.2}$$

https://doi.org/10.1017/jfm.2014.15 Published online by Cambridge University Press

These second-rank tensors are independent of the form (3.1) of the hydrodynamical force $\boldsymbol{F}_h$ on the aggregate; $\boldsymbol{M}_{\boldsymbol{VF}}$ is symmetric positive-definite, while $\boldsymbol{M}_{\boldsymbol{\Omega F}}$ is generic. Let $\boldsymbol{e}_1, \boldsymbol{e}_2, \boldsymbol{e}_3$ be a Cartesian basis with fixed orientation in space and $\boldsymbol{e}_3$ directed upwards. Let $\boldsymbol{e}'_1, \boldsymbol{e}'_2, \boldsymbol{e}'_3$ be another Cartesian basis, rigidly connected to the aggregate; $\boldsymbol{e}'_i = \boldsymbol{e}_i$ at $t = 0$. Three Stokes flow problems for the aggregate are solved at $t = 0$, with $\boldsymbol{T}_h = \boldsymbol{0}$ and the total hydrodynamical force $\boldsymbol{F}_h = \boldsymbol{e}_i$ $(i = 1, 2, 3)$. The velocities $\boldsymbol{V}$ and $\boldsymbol{\Omega}$ from these solutions provide the components $(M'_{\boldsymbol{VF}})_{ij}$ and $(M'_{\boldsymbol{\Omega F}})_{ij}$ of the tensors $\boldsymbol{M}_{\boldsymbol{VF}}$ and $\boldsymbol{M}_{\boldsymbol{\Omega F}}$ in the basis $\boldsymbol{e}'_1, \boldsymbol{e}'_2, \boldsymbol{e}'_3$. As the aggregate moves and rotates, these components are unchanged. So it just remains to make transformations to the fixed basis $\boldsymbol{e}_1, \boldsymbol{e}_2, \boldsymbol{e}_3$. Using (3.1), the dynamics $\mathrm{d}\boldsymbol{e}'_i/\mathrm{d}t = \boldsymbol{\Omega}(t) \times \boldsymbol{e}'_i$ of the orientation vectors $\boldsymbol{e}'_i = E_{ki}(t)\boldsymbol{e}_k$ is described in the fixed basis as

$$\frac{\mathrm{d}E_{ki}}{\mathrm{d}t} = \varepsilon_{jmk}\Omega_j E_{mi}, \quad \Omega_i = NF^S E_{ij}E_{3m}(M'_{\boldsymbol{\Omega F}})_{jm}, \tag{3.3}$$

where ε_{jmk} is the Levi-Civita tensor. These equations are complemented by the dynamics of the translational velocity in the fixed basis:

$$V_i(t) = -NF^S E_{ij}E_{3m}(M'_{\boldsymbol{VF}})_{jm}. \tag{3.4}$$

Since the dynamical solution of the Stokes flow problem is avoided, numerical integration of (3.3) is a very fast way to predict the evolution of the aggregate orientation and approach the long-time sedimentation regime. Note that this beneficial feature is totally lost when a multiparticle cluster is considered in a periodic lattice of other clusters (see Binder *et al.* 2006, 2009).

Still, it is important to complement the numerical integration of (3.3) by analytical results, in order to clarify the nature of the long-time sedimentation regime. For a random multiparticle aggregate with $N \geqslant 4$, steady settling without rotation is not possible. Instead, a steady-state regime with constant angular velocity $\boldsymbol{\Omega}^{st} = (0, 0, \Omega^{st})$ aligned with the gravity vector may be assumed. It immediately follows from (3.1) and (3.2) that, in this regime, the vertical basis vector $\boldsymbol{e}_3$ is the eigenvector of the mobility tensor $\boldsymbol{M}_{\boldsymbol{\Omega F}}$:

$$\boldsymbol{M}_{\boldsymbol{\Omega F}}\boldsymbol{e}_3 = \lambda \boldsymbol{e}_3, \quad \lambda = \frac{\Omega^{st}}{NF^S}. \tag{3.5}$$

It is convenient to solve the eigenvalue problem $\boldsymbol{M}_{\boldsymbol{\Omega F}}\boldsymbol{w} = \lambda \boldsymbol{w}$ once in the basis $\boldsymbol{e}'_1, \boldsymbol{e}'_2, \boldsymbol{e}'_3$ rigidly connected to the aggregate, and normalize the eigenvectors by $\boldsymbol{w}^2 = 1$ (which still defines them to within a sign). The components w'_k are then fixed properties of the aggregate independent of its motion. In the state of steady rotation, the moving basis vectors $\boldsymbol{e}'_1, \boldsymbol{e}'_2, \boldsymbol{e}'_3$ retain constant projections on the vertical axis, which is simply the condition $E_{3k}(t) = w'_k$. Finally, (3.4) gives the steady-state vertical velocity $V^{st} = -V_3$ of the aggregate,

$$V^{st} = NF^S w'_j w'_m (M'_{\boldsymbol{VF}})_{jm}. \tag{3.6}$$

Regarding the appropriate choice of λ, the characteristic equation $\det(\boldsymbol{M}_{\boldsymbol{\Omega F}} - \lambda \boldsymbol{I}) = 0$, as any generic cubic equation with real coefficients, has either one or three real roots. For multiparticle clusters encountered in our growth algorithm (§ 2), both cases are observed, with comparable probabilities when $N \sim 10^2$. However, only one eigenvalue and only one sign choice for the corresponding eigenvector (w'_1, w'_2, w'_3) give a stable regime $E_{3k} = w'_k$ of steady rotation, as confirmed by our numerical integration of (3.3) in the vicinity of all possible steady rotations. However, this unique stable regime, which always exists, is *not* necessarily a global attractor for

https://doi.org/10.1017/jfm.2014.15 Published online by Cambridge University Press

all initial conditions. For a portion of multiparticle clusters built in our simulations, an attachment of a new primary particle and the following rigid-body evolution (3.3) of the new aggregate never resulted in steady rotation, no matter how long the time integration is, and how small the numerical errors (due to the finite time step, multipole truncation, etc.) are made. Modest non-vanishing oscillations of all the components V_i, Ω_i were observed instead. These events, though, were extremely rare: of 8000 aggregates encountered in 80 realizations of the growth process with $N \leqslant 100$ particles and $\varepsilon_{vdW} = 0.005$, just ~ 10 were anomalous, so such occurrences could be safely ignored (see below).

With these considerations in mind, our algorithm works in the following way after a new particle attaches to the aggregate. The orientation dynamics (3.3) is integrated numerically (by the fourth-order Runge–Kutta method) and the eigenvalue λ nearest to $\Omega_3(t)/(NF^S)$ (or the only eigenvalue, if there is one root) is chosen for each time moment t, together with the corresponding eigenvector (w_1', w_2', w_3'). All λ and w_k' are precalculated before integration (3.3), with arbitrary signs for $\boldsymbol{w}$. The regime of steady rotation is reached, once the vector $(E_{31}(t), E_{32}(t), E_{33}(t))$ is close to $\pm(w_1', w_2', w_3')$ (with a tolerance $\sim 10^{-3}$ in the code), which selects the only stable analytical solution $(\lambda, \pm\boldsymbol{w})$ for long-time aggregate sedimentation. This solution also provides the precise steady-state aggregate velocities, both rotational (3.5) and translational (3.6), and the stable orientation (to within an insignificant rotation angle about the vertical axis). This orientation will serve as the initial condition for the aggregate, when the next primary particle is generated below. In exclusive cases (see above), when the aggregate does not reach steady rotation in any reasonable simulation time, the last colliding trajectory is undone and we generate additional trajectories with random initial particle positions until a new acceptable colliding trajectory is found.

The analytical description also helps us to clarify the character of long-time translational motion (which plays the key role in the algorithm of aiming particle–cluster trajectories described in § 4). While the vertical velocity V_3 of the aggregate centre of mass is constant (3.6) in steady rotation, the horizontal components V_1 and V_2 continue periodic oscillations. Remarkably, though, for any rigid body of generic shape, including all our aggregates with $N \geqslant 4$ particles, there is the *axis of steady rotation* (ASR) rigidly connected to the body, such that the long-time sedimentation of the aggregate is simply the circular motion around this axis with angular velocity $(0, 0, \Omega^{st})$, combined with vertical settling. Not only does this axis not contain the centre of mass, but, for most of our aggregates, it is quite away from this centre. Points $\boldsymbol{O}_R$ of this axis are characterized by purely vertical motion, which gives

$$[-\boldsymbol{M}_{VF}\boldsymbol{F}_h + (\boldsymbol{M}_{\Omega F}\boldsymbol{F}_h) \times (\boldsymbol{O}_R - \boldsymbol{O}_g)] \times \boldsymbol{F}_h = 0 \tag{3.7}$$

using (3.2). In steady rotation, $\boldsymbol{F}_h$ is proportional to the normalized eigenvector $\boldsymbol{w}$, so (3.7) may be written as

$$\lambda(\boldsymbol{I} - \boldsymbol{w}\boldsymbol{w})(\boldsymbol{O}_R - \boldsymbol{O}_g) = (\boldsymbol{M}_{VF}\boldsymbol{w}) \times \boldsymbol{w}, \tag{3.8}$$

which defines the ASR, to within an insignificant shift along $\boldsymbol{w}$. Equation (3.8) is the intrinsic description of this axis relative to the aggregate, irrespective of its orientation and position in space. For small λ, the distance $\sim\lambda^{-1}$ from the centre of mass $\boldsymbol{O}_g$ to the axis may be large, even greatly exceeding the aggregate size. However, a large radius of rotation in such cases is compensated by a small magnitude of $\Omega^{st} \sim \lambda$ (see (3.5)), so irregularities in the linear velocity distribution in the aggregate are not observed. In a less extreme example for an aggregate of 37 spheres (figure 2) taken from our simulations of § 8, the ASR (solid line) is still quite away from the

https://doi.org/10.1017/jfm.2014.15 Published online by Cambridge University Press

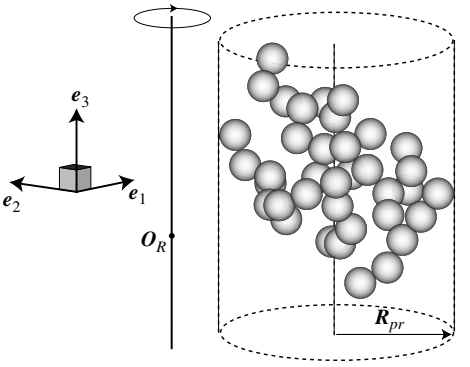


FIGURE 2. A cluster of $N = 37$ particles in steady sedimentation; the solid line is the axis of steady rotation. The bounding cylinder used in the aiming algorithm of § 4 is also shown.

aggregate; the steady-state translational and rotational velocities are $V^{st} = 6.68U^S$ and $\Omega^{st} = -1.87 \times 10^{-2}U^S/a$.

Our analytical description of the steady sedimentation regime through the eigenvalue problem for the coupling tensor $\boldsymbol{M}_{\boldsymbol{\Omega F}}$ applies to rigid bodies of generic shape and, however simple, appears to be new. Instead, characterization of rigid-body motion through a viscous fluid has concentrated so far (e.g. Happel & Brenner 1973, chapter 5) on the eigenvalue problem for the self-adjoint positive-definite translation tensor $\boldsymbol{K}$. Inverting $\boldsymbol{K}$ would be enough to predict the settling speed of bodies of special shape sedimenting without rotation – not the general case considered herein.

4. Aiming the particle–cluster relative trajectories

It would be easy to randomly 'glue' a new primary particle directly to the surface of an existing N-particle aggregate. However, such a simplistic approach is inadequate, at least, for sedimenting non-Brownian suspensions, since it does not correspond to the physical situation. Instead, a far more complex methodology has to be pursued, with random generation of initial particle positions far below the aggregate. All our particle–cluster relative trajectories start in the horizontal plane π_∞, with a large enough vertical offset h_∞ from the aggregate mass centre $\boldsymbol{O}_g$ (the choice of h_∞ is discussed below). For an initially homogeneous suspension, all particle positions in the plane π_∞ then have a uniform probability density, which makes the problem well defined. However, only initial particle centre positions in the small 'interception area' $S_\infty \subset \pi_\infty$ lead to collision with the aggregate. Instead of S_∞, which is infeasible to find exactly in the present problem, we work in a larger domain $\overline{S}_\infty \supset S_\infty$. The overall efficiency of the calculations is strongly affected by how closely $\overline{S}_\infty$ approximates S_∞: too large areas $\overline{S}_\infty$ lead to a large number of wasted trajectories missing the target in the trial-and-error scheme. On the other hand, the construction of $\overline{S}_\infty$ should remain computationally efficient, in order not to place a burden on the entire simulation. In the construction of $\overline{S}_\infty$, it is essential to include the aggregate motion around the ASR. The rotational velocity Ω^{st} (positive or negative) is always much smaller than U^S/a, but the linear horizontal velocity of the aggregate centre $\boldsymbol{O}_g$ due to rotation is typically $(0.3\text{–}0.4)U^S$, and often $(0.5\text{–}0.6)U^S$, because of a large rotation radius; this velocity is particularly important for large initial offsets h_∞. In a way, the difficulties

https://doi.org/10.1017/jfm.2014.15 Published online by Cambridge University Press

of aiming the particle–cluster relative trajectories in this problem may be compared to shooting a fractal-like moving and rotating target from a large distance.

Among several possibilities tested, we found the following method of generating $\bar{S}_\infty$ to be the most successful. In the far-field approximation, the aggregate is unaffected by the particle and undergoes downward spiral motion around the ASR. The hydrodynamical field generated by the aggregate is approximated as the stokeslet contribution from the aggregate centre $\boldsymbol{O}_g$, due to the zero-torque condition (3.1). In the simplest approximation, the particle moves by this velocity field, in addition to downward sedimentation. Let (y_1, y_2, y_3) be a coordinate system rigidly connected to the aggregate, with the origin $\boldsymbol{y} = \boldsymbol{0}$ on the ASR and the y_3 axis directed upwards. In these coordinates, the aggregate centre is $\boldsymbol{O}_g = (R_{SR}, 0, 0)$ (see figure 3); from (3.8), the rotation radius is $R_{SR} = |(\boldsymbol{M}_{VF}\boldsymbol{w}) \times \boldsymbol{w}/\lambda|$. So, the motion of the particle centre relative to this reference frame is approximately described by

$$\frac{\mathrm{d}\boldsymbol{y}}{\mathrm{d}t} = (V^{st} - U^S)\boldsymbol{e}_3 - \frac{1}{8\pi\mu}\left[\frac{\boldsymbol{F}_h}{\xi} + \frac{(\boldsymbol{\xi}\cdot\boldsymbol{F}_h)\boldsymbol{\xi}}{\xi^3}\right] - \boldsymbol{\Omega}^{st}\times\boldsymbol{y}, \tag{4.1}$$

with $\boldsymbol{\xi} = \boldsymbol{y} - \boldsymbol{O}_g$ and $\boldsymbol{\Omega}^{st} = (0, 0, \Omega^{st})$. To complete the $O(\xi^{-1})$ approximation (4.1), it would be logical to add the effect of the primary particle stresslet on the cluster velocity; to this end, the hydrodynamical force $\boldsymbol{F}_h$ is simply modified in (4.1) by a factor of $(N-1)/N$. This possible refinement, though (noticeable at small N only), was safely neglected in our aiming algorithm. Equation (4.1) is only used to build the bounding domain $\bar{S}_\infty$ around the true interception area S_∞ and does not have to be precise. Let

$$R_h = \frac{|\boldsymbol{F}_h|}{6\pi\mu V^{st}} = \frac{aNU^S}{V^{st}} \tag{4.2}$$

be the 'hydrodynamical radius' of the aggregate. To determine when a trajectory (4.1), starting from $y_3 = -h_\infty$, can reach the aggregate centre to within a distance $R \sim R_h$ (the choice of R is discussed below), many such trajectories (5000 in the code) are numerically integrated backwards from the lower hemisphere $|\boldsymbol{y} - \boldsymbol{O}_g| = R$, $y_3 < 0$ until intersection with the plane $y_3 = -h_\infty$ (figure 3). The end points of these trajectories in π_∞ sweep a domain usually close to a circle. The minimal circle around all the end points (constructed with sufficient accuracy in a simple manner, appendix A) serves as $\bar{S}_\infty$ (figure 3) in the reference frame (y_1, y_2, y_3). For the aggregate orientation in the state of steady rotation, prepared as the initial condition to continue the simulation (§ 3), it remains to match the reference frame (y_1, y_2, y_3) as shown in figure 3, which gives the bounding circle $\bar{S}_\infty$ relative to the aggregate. The next step of the algorithm is to generate random initial particle positions in $\bar{S}_\infty$ only, with uniform probability density, and solve the full hydrodynamical problem for the particle–cluster relative motion, until a colliding trajectory is found.

Since the approximate scheme (4.1) ignores the true particle–cluster hydrodynamical interactions, it is generally expected, for $R \sim R_h$, to greatly overestimate the collision efficiency, thus making $\bar{S}_\infty$ a much larger area than S_∞. For the efficiency of the algorithm, R must be made as small as possible, with $\bar{S}_\infty$ still embracing *all* possible initial conditions leading to particle–cluster collision. One lower limitation on R is that all the trajectories (4.1) should enter the hemisphere $|\boldsymbol{y} - \boldsymbol{O}_g| = R$, $y_3 < 0$ from outside, i.e. $\boldsymbol{\xi}\cdot\mathrm{d}\boldsymbol{y}/\mathrm{d}t < 0$ (thus enabling backward integration to $y_3 = -h_\infty$). For our clusters (§ 8), the rotational term $\boldsymbol{\Omega}^{st}\times\boldsymbol{y}$ is small compared to the other terms in (4.1) when $|\boldsymbol{\xi}| \sim R_h$, so the limitation $\boldsymbol{\xi}\cdot\mathrm{d}\boldsymbol{y}/\mathrm{d}t < 0$ yields

$$R > R_{crit}, \quad R_{crit} = \frac{|\boldsymbol{F}_h|}{4\pi\mu(V^{st} - U^S)} = \frac{3}{2}\frac{V^{st}}{(V^{st} - U^S)}R_h. \tag{4.3}$$

https://doi.org/10.1017/jfm.2014.15 Published online by Cambridge University Press

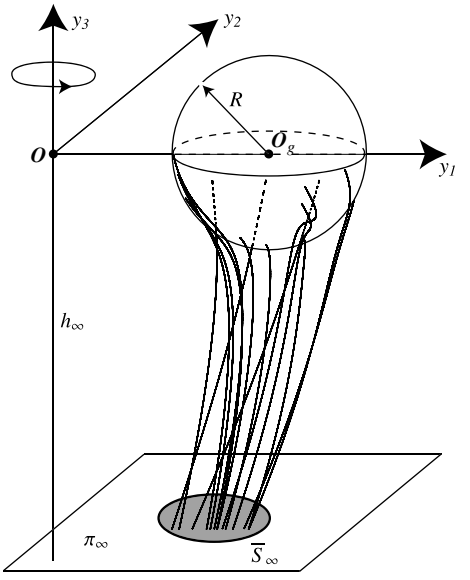


FIGURE 3. Schematic for aiming particle–cluster relative trajectories (not to scale).

The condition $R > R_{crit}$, though, is not enough for $\overline{S}_\infty$ to contain all the interception area S_∞, except for the case of small-size clusters. With R slightly above R_{crit}, some particle–cluster relative trajectories starting outside $\overline{S}_\infty$ were still observed to result in collision when the full hydrodynamical problem is solved.

For a better rule, consider the minimal cylinder surrounding the whole aggregate surface in the state of steady rotation, with the vertical axis of symmetry of the cylinder passing through the aggregate centre $\boldsymbol{O}_g$ (figure 2); let R_{pr} be the cylinder base radius. A successful empirically tested universal expression for R in our problem is found to be

$$R = \max(1.1R_{crit},\ \ R_{pr} + 1.5a). \tag{4.4}$$

Although it is not possible to prove analytically that the choice (4.4) results in no collisions for all initial conditions outside $\overline{S}_\infty$, this fact was confirmed by extensive calculations. To this end, our cluster growth simulations (§ 8) were interrupted tens of times, with N from 2 to 50, to verify that the collision with an aggregate is never observed when a particle relative trajectory starts anywhere on the contour of $\overline{S}_\infty$ (40 points evenly spaced along the contour were tested). The minimum particle–cluster surface clearance for each of these missing trajectories was typically $0.5a$–a, and in just a few cases as small as $0.05a$ (still well outside the range of action of van der Waals forces). So, the true interception area S_∞ never crosses the contour of $\overline{S}_\infty$ and is all strictly inside $\overline{S}_\infty$. The empirical rule (4.4) turns out to be not far from optimal. It should be emphasized that the choice of R only affects the computational efficiency and not the results (upon ensemble averaging over many growth realizations) as long as $S_\infty \subset \overline{S}_\infty$.

For the initial particle motion to be totally unaffected by the aggregate, the initial offset h_∞ should have been much larger than the outer radius R_{out} of the aggregate, which is too restrictive for large N and would limit the practical relevance of the present theory. Fortunately, it is legitimate to start relative trajectories from much closer separations, with the particle position probability density still being uniform

https://doi.org/10.1017/jfm.2014.15 Published online by Cambridge University Press

in π_∞ (the principal assumption behind the present algorithm). Indeed, the Liouville equation $\partial P/\partial t + \boldsymbol{\nabla} \cdot (P\boldsymbol{V}_{rel}) = 0$, with $\boldsymbol{V}_{rel}$ being the particle relative velocity and P being the volume probability density in the reference frame rigidly connected to the aggregate, allows for the uniform solution $P = \text{const.}$, if $\boldsymbol{V}_{rel}$ is divergence-free. The complete $O(\xi^{-1})$ far-field approximation to $\boldsymbol{V}_{rel}$ (see the remarks above) is solenoidal. The difference $\Delta\boldsymbol{V}_{rel}$ between our numerical $\boldsymbol{V}_{rel}$ (with full hydrodynamical interactions) and the $O(\xi^{-1})$ approximation, responsible for $\boldsymbol{\nabla} \cdot \boldsymbol{V}_{rel}$, is observed to scale like $O(V^{st}a^2/(|\boldsymbol{\xi}| - R_{out})^2)$ for both small and large N. This scaling requires the centre-to-centre distance $|\boldsymbol{\xi}|$ to be much larger than a and just several times larger than the cluster outer radius R_{out}. Hence, from the Liouville equation, the conditional probability density P is uniform in this range, at least to within $O(a^2/(|\boldsymbol{\xi}| - R_{out})^2)$. Based on these estimations, it was sufficient to set

$$h_\infty = 3R_h + 100a \tag{4.5}$$

in all our simulations with $N \leqslant 100$; $3R_h$ always exceeds R_{out}. Note that the above arguments based on the Liouville equation are reminiscent of the far-field analysis of the pair distribution function in dilute suspensions (e.g. Cox & Brenner 1971; Batchelor 1972; Batchelor & Green 1972).

For $N = 3$ and 2 (with vertical initial doublet alignment), the same aiming strategy applies, with $\boldsymbol{\Omega}^{st} = \boldsymbol{0}$ and R_{SR} arbitrary. In all other cases $N \geqslant 4$, though, it was critical to retain the rotational term $\boldsymbol{\Omega}^{st} \times \boldsymbol{y}$ in backward integrations of (4.1); otherwise, a successful aiming strategy could not be achieved, even for much smaller initial offsets than (4.5). We have not fully tested yet if it would be sufficient to integrate (4.1) backwards from the perimeter $y_3 = 0$ only, instead of the whole hemisphere $|\boldsymbol{\xi}| = R$, $y_3 \leqslant 0$ to obtain $\overline{S}_\infty$. Our algorithm does not rely on this simplification.

Even though the choice (4.4) for R is close to optimal, the true interception area S_∞ is still a small subset of $\overline{S}_\infty$, which was the main difficulty in the present simulations. Figure 4 gives an idea of how many particle–cluster relative trajectories were necessary in our calculations of § 8 for moderate van der Waals attraction, $\varepsilon_{vdW} = 0.005$. Each point shows the number of trajectories N_{tr} that had to be generated for a cluster of mass N to attach a new particle, on the average for 80 process realizations. For $N \sim O(10^2)$, this number of trajectories shows only a slight upward trend with N, remaining around 45. The dispersion is very strong, though, owing to the fractal-like structures of the aggregates: in individual cases, from several to several hundred trajectories had to be generated. The total number of trajectories in all 80 realizations with all $N \leqslant 99$ was 290 000. Extensive calculations of this kind require a highly efficient hydrodynamical algorithm, as described in the next section.

Unless otherwise stated, all the present simulations assume the vertical initial orientation of doublets. Still, it is useful to note that, in the case of a random initial orientation, the above aiming algorithm for $N = 2$ must be modified. An isolated doublet of equal spheres, with the angle $0 < \theta < \pi/2$ between the centreline and the vertical, settles without rotation at the vertical speed $V^{st} = U^S(1.550 \cos^2\theta + 1.380 \sin^2\theta)$, but it also has a small horizontal velocity $V_{hor} = 0.170U^S \cos\theta \sin\theta$, owing to the difference between the hydrodynamical mobility coefficients (per particle) 1.550 and 1.380 for the doublet motion along and normal to the line of centres, respectively. The centre-to-centre vector from the top sphere to the bottom sphere in the doublet, when projected on the horizontal plane, gives the direction of $\boldsymbol{V}_{hor}$. It is easy to interpret this horizontal velocity $\boldsymbol{V}_{hor}$ as a result of an infinitesimally slow aggregate rotation about ASR with an angular velocity $(0, 0, \Omega^{st})$ and rotation radius R_{SR}, so that $\Omega^{st} \to 0$, $R_{SR} \to \infty$ and $\Omega^{st}R_{SR} = V_{hor}$. This way, the above aiming algorithm can be used as is for $N = 2$, with R_{SR} artificially set to $(10^5$–$10^6)a$. Slight

https://doi.org/10.1017/jfm.2014.15 Published online by Cambridge University Press

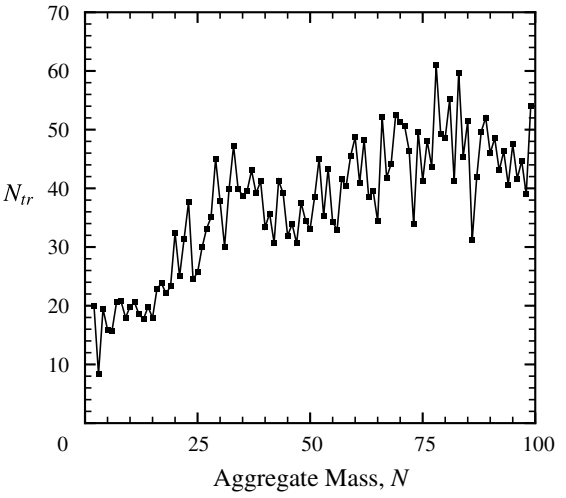


FIGURE 4. The number of relative trajectories required for a cluster of mass N to attach a new primary particle; for every N, the results are averaged over 80 cluster growth realizations with moderate van der Waals attraction $\varepsilon_{vdW} = 0.005$.

readjustment of (4.4) (with 1.2 instead of 1.1) was found to be necessary in the case of random initial orientations, for $\overline{S}_\infty$ to embrace all possible collisions of the doublet with the third particle.

5. Solution of the hydrodynamical problems

Below, we describe our solution method for a rigid cluster of N spheres in the presence of another, $(N+1)$th, primary particle in a quiescent unbounded liquid; simplifications for an isolated cluster are discussed at the end of this section. Let $\boldsymbol{x}^1, \ldots, \boldsymbol{x}^{N+1}$ be the centres of all spheres $S_1, \ldots, S_{N+1}$ in the system. At each configuration, the total hydrodynamical force $\boldsymbol{F}_h^{agg}$ and torque $\boldsymbol{T}_h^{agg}$ acting on the cluster (aggregate) and the force $\boldsymbol{F}_h^p$ and torque $\boldsymbol{T}_h^p$ acting on the primary particle are prescribed by the balance equations

$$\boldsymbol{F}_h^{agg} = -\boldsymbol{F}_{ext}^{agg}, \quad \boldsymbol{T}_h^{agg} = -\boldsymbol{T}_{ext}^{agg} \tag{5.1}$$

and

$$\boldsymbol{F}_h^p = -\boldsymbol{F}_{ext}^p, \quad \boldsymbol{T}_h^p = -\boldsymbol{T}_{ext}^p, \tag{5.2}$$

with the external forces and torques

$$\boldsymbol{F}_{ext}^{agg} = -NF^S\boldsymbol{e}_3 + \sum_{\alpha=1}^{N}(\boldsymbol{F}_{vdW})_{\alpha,N+1}, \quad \boldsymbol{T}_{ext}^{agg} = \sum_{\alpha=1}^{N}\boldsymbol{r}_\alpha \times (\boldsymbol{F}_{vdW})_{\alpha,N+1} \tag{5.3}$$

and

$$\boldsymbol{F}_{ext}^p = -F^S\boldsymbol{e}_3 - \sum_{\alpha=1}^{N}(\boldsymbol{F}_{vdW})_{\alpha,N+1}, \quad \boldsymbol{T}_{ext}^p = 0, \tag{5.4}$$

respectively. Here, $(\boldsymbol{F}_{vdW})_{\alpha,N+1}$ is the molecular force (see § 1) acting on the cluster particle α from particle $N+1$ (assuming usual pairwise additivity for these short-range

https://doi.org/10.1017/jfm.2014.15 Published online by Cambridge University Press

attractions). The torques $\boldsymbol{T}_h^{agg}$ and $\boldsymbol{T}_{ext}^{agg}$ are calculated about the aggregate centre $\boldsymbol{O}_g$, and $\boldsymbol{r}_\alpha = \boldsymbol{x}^\alpha - \boldsymbol{O}_g$ are the particle positions relative to this centre. For the primary particle, the torques are taken about $\boldsymbol{x}^{N+1}$. Of course, the solution method is independent of the particular forms (5.3) and (5.4).

Given $\boldsymbol{F}_h^{agg}$, $\boldsymbol{T}_h^{agg}$, $\boldsymbol{F}_h^p$ and $\boldsymbol{T}_h^p$, the problem is to determine the instantaneous grand velocity vector $\boldsymbol{W} = (\boldsymbol{V}^{agg}, \boldsymbol{\Omega}^{agg}, \boldsymbol{V}^p, \boldsymbol{\Omega}^p)$ to predict the system dynamics. This 12-vector includes translational velocities $\boldsymbol{V}^{agg}$ and $\boldsymbol{V}^p$ of the aggregate and particle centres $\boldsymbol{O}_g$, $\boldsymbol{x}^{N+1}$, as well as the rotational velocities $\boldsymbol{\Omega}^{agg}$ and $\boldsymbol{\Omega}^p$ for the aggregate and the particle.

5.1. *Geometry perturbation*

The multipole solution does not suffer from (virtually) zero surface clearance between the cluster particles forming a contact network, because there is no lubrication in rigid-body motion. In contrast, when the primary particle closely approaches the cluster, a straightforward approach would require a prohibitively large order of multipoles to account for particle–cluster lubrication. To overcome this difficulty and still have a highly accurate solution, we apply the idea of *geometry perturbation* first proposed by Zinchenko (1998) in conductivity simulations through a packed bed with highly conductive inclusions (where the near-contact solution behaviour is also singular). In the present context, the first step is to reduce the original radius a of only one, primary particle S_{N+1} (figure 5) to $\widehat{a}$ ($\approx a$) just enough for an acceptable convergence rate of the multipole solution. This rate is measured by the maximum allowed progression exponent $q_{max} < 1$. Even for multiparticle interactions, this exponent is proven to be controlled by two-particle interactions and is a geometric quantity, no matter if the Stokes or Laplace problem is solved (Zinchenko 1994). Prior to shrinkage, the system is monodisperse and the progression exponents from $S_\alpha \leftrightarrow S_{N+1}$ interaction limiting the convergence are (Zinchenko 1994)

$$q_\alpha = \frac{1}{2}\left\{\frac{\ell_\alpha}{a} - \left[\left(\frac{\ell_\alpha}{a}\right)^2 - 4\right]^{1/2}\right\} \approx 1 - \left(\frac{\ell_\alpha - 2a}{a}\right)^{1/2}, \tag{5.5}$$

where $\ell_\alpha = |\boldsymbol{x}^\alpha - \boldsymbol{x}^{N+1}|$. Simplification is made on the right-hand side of (5.5) for near-contact $\ell_\alpha \approx 2a$. Note the strong sensitivity of q_α to small surface clearances $\ell_\alpha - 2a$. There may be one or more cluster particles with q_α above the acceptable level q_{max}, i.e. with

$$\ell_\alpha/a < 2 + (1 - q_{max})^2. \tag{5.6}$$

All such particles form a set $\mathscr{L}$ and, by definition, *lubrication pairs* $(\alpha, N+1)$, $\alpha \in \mathscr{L}$ with the primary particle. After shrinkage of S_{N+1} to $\widehat{S}_{N+1}$, the system is (slightly) polydisperse, and the progression exponents $\widehat{q}_\alpha$ from $S_\alpha \leftrightarrow \widehat{S}_{N+1}$ interaction limiting the convergence on the primary particle become (Zinchenko *et al.* 2011)

$$\begin{aligned}\widehat{q}_\alpha &= \frac{\ell_\alpha^2 + \widehat{a}^2 - a^2 - \{[\ell_\alpha^2 - (\widehat{a}+a)^2][\ell_\alpha^2 - (\widehat{a}-a)^2]\}^{1/2}}{2\ell_\alpha \widehat{a}} \\ &\approx 1 - \left[\frac{2(\ell_\alpha - \widehat{a} - a)a}{\widehat{a}(\widehat{a}+a)}\right]^{1/2}.\end{aligned} \tag{5.7}$$

https://doi.org/10.1017/jfm.2014.15 Published online by Cambridge University Press

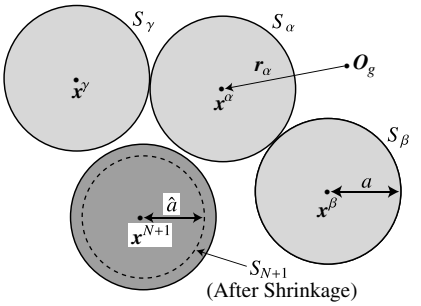


FIGURE 5. A schematic of geometry perturbation for a primary particle (dark shading) closely interacting with a rigid cluster (light shading) of mass N; only nearby cluster particles are shown. In actual calculations, the perturbation is only applied for much smaller particle–cluster separations, and is much smaller than shown.

Again, simplification has been made in (5.7) for near-contact. Using (5.7), it is easy to find the maximum possible $\widehat{a}$, which makes all $\widehat{q}_\alpha \leqslant q_{max}$. For a typical $q_{max} = 0.9$, the geometry perturbation is not in effect ($\widehat{a} = a$) until the particle comes very close to the cluster, and is always much smaller than shown schematically in figure 5.

In order for the Stokes flow solution in the new geometry ($S_1, \ldots, S_N, \widehat{S}_{N+1}$) to provide the same (to high accuracy) grand velocity vector $\boldsymbol{W}$ as in the original problem, the force and torque balances must be modified for the new geometry. Akin to Zinchenko (1998), we note that the difference between the total hydrodynamical force/torque acting on the aggregate and the sum of singular gap contributions from all the lubrication pairs comes from the 'outer solution'. Hence, for the motion with the same $\boldsymbol{W}$, this difference must be insensitive to whether it is calculated in the original or modified geometry; the same is true for the hydrodynamical force/torque acting on the primary particle. Prior to shrinkage, the cumulative gap contributions from the lubrication pairs to the total hydrodynamical forces and torques can be written as

$$(\boldsymbol{F}^{agg}_{sing}, \boldsymbol{T}^{agg}_{sing}, \boldsymbol{F}^{p}_{sing}, \boldsymbol{T}^{p}_{sing}) = (\boldsymbol{R}^{agg}_{\boldsymbol{F}}, \boldsymbol{R}^{agg}_{\boldsymbol{T}}, \boldsymbol{R}^{p}_{\boldsymbol{F}}, \boldsymbol{R}^{p}_{\boldsymbol{T}})\boldsymbol{W}. \tag{5.8}$$

After shrinkage, we have

$$(\widehat{\boldsymbol{F}}^{agg}_{sing}, \widehat{\boldsymbol{T}}^{agg}_{sing}, \widehat{\boldsymbol{F}}^{p}_{sing}, \widehat{\boldsymbol{T}}^{p}_{sing}) = (\widehat{\boldsymbol{R}}^{agg}_{\boldsymbol{F}}, \widehat{\boldsymbol{R}}^{agg}_{\boldsymbol{T}}, \widehat{\boldsymbol{R}}^{p}_{\boldsymbol{F}}, \widehat{\boldsymbol{R}}^{p}_{\boldsymbol{T}})\boldsymbol{W}. \tag{5.9}$$

Note that (5.8) and (5.9) use the same lubrication pairs defined by (5.6). The 3×12 matrices $\boldsymbol{R}^{agg}_{\boldsymbol{F}}, \ldots, \boldsymbol{R}^{p}_{\boldsymbol{T}}$ are derived from the well-known asymptotic solutions for two equal spheres S_α and S_{N+1} of radius a in near-contact. To derive $\widehat{\boldsymbol{R}}^{agg}_{\boldsymbol{F}}, \ldots, \widehat{\boldsymbol{R}}^{p}_{\boldsymbol{T}}$, the more general asymptotic solutions of Cooley & O'Neill (1969) and O'Neill & Majumdar (1970) for unequal spheres S_α and $\widehat{S}_{N+1}$ are used. All the matrices $\boldsymbol{R}^{agg}_{\boldsymbol{F}}, \ldots, \widehat{\boldsymbol{R}}^{p}_{\boldsymbol{T}}$ contain terms inversely proportional to the surface clearances, and logarithmic terms.

From (5.8) and (5.9), the modified force/torque balances for the new geometry are simply

$$\widehat{\boldsymbol{F}}^{agg}_{h} + (\boldsymbol{R}^{agg}_{\boldsymbol{F}} - \widehat{\boldsymbol{R}}^{agg}_{\boldsymbol{F}})\boldsymbol{W} = \boldsymbol{F}^{agg}_{h}, \quad \widehat{\boldsymbol{T}}^{agg}_{h} + (\boldsymbol{R}^{agg}_{\boldsymbol{T}} - \widehat{\boldsymbol{R}}^{agg}_{\boldsymbol{T}})\boldsymbol{W} = \boldsymbol{T}^{agg}_{h} \tag{5.10}$$

https://doi.org/10.1017/jfm.2014.15 Published online by Cambridge University Press

and

$$\widehat{\boldsymbol{F}}_h^p + (\boldsymbol{R}_{\boldsymbol{F}}^p - \widehat{\boldsymbol{R}}_{\boldsymbol{F}}^p)\boldsymbol{W} = \boldsymbol{F}_h^p, \quad \widehat{\boldsymbol{T}}_h^p + (\boldsymbol{R}_{\boldsymbol{T}}^p - \widehat{\boldsymbol{R}}_{\boldsymbol{T}}^p)\boldsymbol{W} = \boldsymbol{T}_h^p. \tag{5.11}$$

The right-hand sides of (5.10) and (5.11) are prescribed by (5.1) and (5.2); the original external forces/torques (5.3) and (5.4) *should not* be modified. The explicit forms of matrices $\boldsymbol{R}_{\boldsymbol{F}}^{agg} - \widehat{\boldsymbol{R}}_{\boldsymbol{F}}^{agg}$, etc. are listed in appendix B. Since $\widehat{a} \leqslant a$, all these matrices (when non-zero) form a negative-definite grand lubrication resistance matrix (12×12), and the problem (5.10)–(5.11) is well posed.

It must be emphasized that the primary particle radius reduction is just a temporary tool to solve the original hydrodynamical problem for *any* original particle–cluster surface clearances, however small; in all the rest of our code, the original radius a is used for S_{N+1}. The correctness of this geometry perturbation technique and insensitivity of the results to the choice of $q_{max} \geqslant 0.9$ are demonstrated in § 7.

5.2. *Multipole solution*

Assuming that $\widehat{S}_{N+1}$ is now used for S_{N+1}, the next step, standard for a cloud of spheres in an unbounded medium, is to represent the fluid velocity $\boldsymbol{u}(\boldsymbol{x})$ as a sum of singular contributions from all the particle centres,

$$\boldsymbol{u}(\boldsymbol{x}) = \sum_{\beta=1}^{N+1} \boldsymbol{u}_-^\beta(\boldsymbol{x} - \boldsymbol{x}^\beta), \tag{5.12}$$

using Lamb's (Happel & Brenner 1973) singular series,

$$\begin{aligned}\boldsymbol{u}_-^\beta(\boldsymbol{r}) \;=\; \sum_{\nu=1}^{\infty} \Bigg[& \nabla \times (\boldsymbol{r}\chi_{-(\nu+1)}^\beta) + \nabla \Phi_{-(\nu+1)}^\beta \\ & - \frac{(\nu-2) r^2 \nabla p_{-(\nu+1)}^\beta}{2\nu(2\nu-1)} + \frac{(\nu+1) p_{-(\nu+1)}^\beta \boldsymbol{r}}{\nu(2\nu-1)} \Bigg].\end{aligned} \tag{5.13}$$

The negative-order solid harmonics are

$$\left.\begin{aligned} p_{-(\nu+1)}^\beta(\boldsymbol{r}) &= \sum_{m=-\nu}^{\nu} A_{-(\nu+1),m}^\beta \left(\frac{a_\beta}{r}\right)^{\nu+1} Y_{\nu,m}(\boldsymbol{r}), \\ \Phi_{-(\nu+1)}^\beta(\boldsymbol{r}) &= \sum_{m=-\nu}^{\nu} B_{-(\nu+1),m}^\beta \left(\frac{a_\beta}{r}\right)^{\nu+1} Y_{\nu,m}(\boldsymbol{r}), \\ \chi_{-(\nu+1)}^\beta(\boldsymbol{r}) &= \sum_{m=-\nu}^{\nu} C_{-(\nu+1),m}^\beta \left(\frac{a_\beta}{r}\right)^{\nu+1} Y_{\nu,m}(\boldsymbol{r}). \end{aligned}\right\} \tag{5.14}$$

Here, $a_\beta = a$ for $\beta \leqslant N$, and $a_{N+1} = \widehat{a}$; and $Y_{\nu,m}$ are standard normalized spherical harmonics. The as-yet unknown complex coefficients in (5.14) obey

$$A_{-(\nu+1),m}^\beta = (-1)^m \overline{A}_{-(\nu+1),-m}^\beta, \quad \text{etc.} \tag{5.15}$$

To exploit the kinematic boundary conditions on a sphere S_α (either a primary particle or in the cluster), singular contributions (5.12) from all $\beta \neq \alpha$ must be

https://doi.org/10.1017/jfm.2014.15 Published online by Cambridge University Press

re-expanded near S_α in Lamb's regular form,

$$\boldsymbol{u}_+^\alpha(\boldsymbol{x}) = \sum_{n=1}^{\infty} \left[\nabla \times (\boldsymbol{r}\chi_n^\alpha) + \nabla \Phi_n^\alpha + \frac{(n+3)r^2 \nabla p_n^\alpha}{2(n+1)(2n+3)} - \frac{n p_n^\alpha \boldsymbol{r}}{(n+1)(2n+3)} \right], \tag{5.16}$$

with $\boldsymbol{r} = \boldsymbol{x} - \boldsymbol{x}^\alpha$ and positive-order solid harmonics

$$\left.\begin{aligned} p_n^\alpha(\boldsymbol{r}) &= \sum_{m=-n}^{n} A_{n,m}^\alpha \left(\frac{r}{a_\alpha}\right)^n Y_{n,m}(\boldsymbol{r}), \\ \Phi_n^\alpha(\boldsymbol{r}) &= \sum_{m=-n}^{n} B_{n,m}^\alpha \left(\frac{r}{a_\alpha}\right)^n Y_{n,m}(\boldsymbol{r}), \\ \chi_n^\alpha(\boldsymbol{r}) &= \sum_{m=-n}^{n} C_{n,m}^\alpha \left(\frac{r}{a_\alpha}\right)^n Y_{n,m}(\boldsymbol{r}). \end{aligned}\right\} \tag{5.17}$$

For each term of (5.12), the general explicit re-expansion formulae from $A_{-(\nu+1),m}^\beta$, etc. to $A_{n,m}^\alpha$, etc. exist (Mo & Sangani 1994; Filippov 2000), but they are quite complicated. This re-expansion operation is equally cumbersome when a different set of basis vector functions (e.g. Cichocki, Felderhof & Schmitz 1988) is used (other than Lamb's representations). The cost of each re-expansion from $\boldsymbol{u}_-^\beta$ to $\boldsymbol{u}_+^\alpha$ is still $O(L^4)$, where $L \geqslant \nu$, n is the truncation level in (5.13) and (5.16). These explicit re-expansion relations are unavoidable to formulate the system of equations for non-iterative solution. However, for dynamical simulation of multiparticle systems, an iterative solution at each time step is strongly favoured, and an alternative re-expansion technique based on rotational transformation of spherical harmonics is far more efficient. This method harks back to multiparticle conductivity simulations (Zinchenko 1994) and was later extended (Zinchenko & Davis 2000) to hydrodynamical problems. The re-expansion from $A_{-(\nu+1),m}^\beta$, etc. to $A_{n,m}^\alpha$, etc. is done in three steps: (i) choose a temporary 'axial' coordinate system x_1', x_2', x_3' with the x_3' axis along $\boldsymbol{x}^\beta - \boldsymbol{x}^\alpha$ (not to be confused with the coordinate system in § 3) and transform $A_{-(\nu+1),m}^\beta$, etc. from the original basis (the same for all spheres) to $A_{-(\nu+1),m'}^\beta$, etc. in the axial basis; (ii) re-expand from $A_{-(\nu+1),m'}^\beta$, etc. to $A_{n,m'}^\alpha$, etc. in the axial basis; and (iii) transform $A_{n,m'}^\alpha$, etc. back to $A_{n,m}^\alpha$, etc. in the original basis. All these steps are detailed in §3.3 of Zinchenko & Davis (2000). For the coefficients of rotational transformations (known as Wigner functions in the quantum theory of angular momentum) in steps (i) and (ii), though, we use a slightly more complex, but absolutely stable recurrent scheme of Zinchenko (1998). This three-step procedure reduces the re-expansion cost to $O(L^3)$ without any new approximations. Moreover, while n and ν need to be quite large for some pairs (α, β) in the case of close particle–cluster interaction (see below), the azimuthal numbers m' in the axial basis can *always* be limited by $O(1)$ values, $|m'| \leqslant m_{max}$. Increasing m_{max} above 6 never had a perceptible effect in the present calculations. Note that the input $A_{-(\nu+1),m}^\beta$, etc. and output $A_{n,m}^\alpha$, etc. coefficients in the original basis still have all the necessary azimuthal numbers $|m| \leqslant \nu$ and $|m| \leqslant n$, respectively, but the cost of all three re-expansion steps now reduces to $O(L^2)$. One possible explanation why this azimuthal truncation $|m'| \leqslant O(1)$ should be applicable and efficient in a broad class of multiparticle problems, far outside the present application, is that interactions between two spheres moving along and normal to the line of centres, when written in an axial basis, require only $m' = 0$

https://doi.org/10.1017/jfm.2014.15 Published online by Cambridge University Press

and $m' = \pm 1$, respectively. The truncation $|m'| \leqslant O(1)$ was also found to work in a nonlinear three-dimensional problem of collisions between two surfactant-laden spherical drops (Zinchenko *et al.* 2011).

The boundary conditions for $\boldsymbol{u}^\alpha_- + \boldsymbol{u}^\alpha_+$ on S_α are now written in a standard way as

$$\left.\begin{aligned} A^\alpha_{-(n+1),m} &= -\frac{n(2n-1)}{(n+1)}\left[\frac{1}{2}A^\alpha_{n,m} + \frac{2n+1}{a_\alpha^2}B^\alpha_{n,m}\right] + \widetilde{A}^\alpha_{-(n+1),m}, \\ B^\alpha_{-(n+1),m} &= -\frac{n}{2(n+1)}\left[\frac{(2n+1)a_\alpha^2}{2(2n+3)}A^\alpha_{n,m} + (2n-1)B^\alpha_{n,m}\right] + \widetilde{B}^\alpha_{-(n+1),m}, \\ C^\alpha_{-(n+1),m} &= -C^\alpha_{n,m} + \widetilde{C}^\alpha_{-(n+1),m}. \end{aligned}\right\} \tag{5.18}$$

The additional terms $\widetilde{A}^\alpha_{-(n+1),m}$, $\widetilde{B}^\alpha_{-(n+1),m}$ and $\widetilde{C}^\alpha_{-(n+1),m}$ are due to the cluster and primary particle motion, as if in the absence of any interactions. For a cluster particle ($\alpha \leqslant N$), we have

$$\left.\begin{aligned} \widetilde{A}^\alpha_{-2,0} &= \frac{3}{2a_\alpha}\left(\frac{4\pi}{3}\right)^{1/2}(\boldsymbol{V}^{agg} + \boldsymbol{\Omega}^{agg}\times\boldsymbol{r}_\alpha)_3, \\ \widetilde{A}^\alpha_{-2,1} &= \frac{3}{2a_\alpha}\left(\frac{2\pi}{3}\right)^{1/2}[(\boldsymbol{V}^{agg} + \boldsymbol{\Omega}^{agg}\times\boldsymbol{r}_\alpha)_1 - \mathrm{i}(\boldsymbol{V}^{agg} + \boldsymbol{\Omega}^{agg}\times\boldsymbol{r}_\alpha)_2], \\ \widetilde{B}^\alpha_{-2,m} &= \frac{a_\alpha^2}{6}\widetilde{A}^\alpha_{-2,m}, \quad (m = 0,\,1), \\ \widetilde{C}^\alpha_{-2,0} &= \left(\frac{4\pi}{3}\right)^{1/2} a_\alpha \Omega_3^{agg}, \quad \widetilde{C}^\alpha_{-2,1} = \left(\frac{2\pi}{3}\right)^{1/2}(\Omega_1^{agg} - \mathrm{i}\Omega_2^{agg}). \end{aligned}\right\} \tag{5.19}$$

Here, i is the imaginary unit; for $m = -1$, the conjugation rule (5.15) applies; all other additional terms are zero. For the primary particle $\alpha = N+1$, the same relations (5.19) hold, with $\boldsymbol{r}_\alpha = \boldsymbol{0}$ and $\boldsymbol{V}^p$, $\boldsymbol{\Omega}^p$ instead of $\boldsymbol{V}^{agg}$, $\boldsymbol{\Omega}^{agg}$.

To organize (5.18) as an iterative process for $A^\alpha_{-(n+1),m}$, etc., the as-yet unknown grand velocity vector $\boldsymbol{W}$ must first be excluded. The hydrodynamical force $-4\pi\mu\nabla(r^3 p^\alpha_{-2})$ and torque $-8\pi\mu\nabla(r^3\chi^\alpha_{-2})$ (about $\boldsymbol{x}^\alpha$) acting on an individual sphere are used to form $\widehat{\boldsymbol{F}}^{agg}_h$ and $\widehat{\boldsymbol{T}}^{agg}_h$ for the entire aggregate. By the partition (5.18), each of these quantities, as well as $\widehat{\boldsymbol{F}}^p_h$ and $\widehat{\boldsymbol{T}}^p_h$, is written as a part ($\widehat{\boldsymbol{F}}^{agg}_o$, $\widehat{\boldsymbol{T}}^{agg}_o$, $\widehat{\boldsymbol{F}}^p_o$, $\widehat{\boldsymbol{T}}^p_o$) as if independent of $\boldsymbol{W}$, plus an additional part due to (5.19); the additional part simply corresponds to the motion of non-interacting spheres. With further simplifications due to equal particle radii in the cluster, the modified force and torque balances (5.10)–(5.11) are recast as

$$\left.\begin{aligned} &\widehat{\boldsymbol{F}}^{agg}_o - 6\pi\mu a N\boldsymbol{V}^{agg} + (\boldsymbol{R}^{agg}_{\boldsymbol{F}} - \widehat{\boldsymbol{R}}^{agg}_{\boldsymbol{F}})\boldsymbol{W} = \boldsymbol{F}^{agg}_h, \\ &\widehat{\boldsymbol{T}}^{agg}_o - \left[6\pi\mu a\sum_{\alpha=1}^{N}(r_\alpha^2\boldsymbol{I} - \boldsymbol{r}_\alpha\boldsymbol{r}_\alpha) + 8\pi\mu a^3 N\right]\boldsymbol{\Omega}^{agg} + (\boldsymbol{R}^{agg}_{\boldsymbol{T}} - \widehat{\boldsymbol{R}}^{agg}_{\boldsymbol{T}})\boldsymbol{W} = \boldsymbol{T}^{agg}_h, \\ &\widehat{\boldsymbol{F}}^p_o - 6\pi\mu\widehat{a}\boldsymbol{V}^p + (\boldsymbol{R}^p_{\boldsymbol{F}} - \widehat{\boldsymbol{R}}^p_{\boldsymbol{F}})\boldsymbol{W} = \boldsymbol{F}^p_h, \\ &\widehat{\boldsymbol{T}}^p_o - 8\pi\mu\widehat{a}^3\boldsymbol{\Omega}^p + (\boldsymbol{R}^p_{\boldsymbol{T}} - \widehat{\boldsymbol{R}}^p_{\boldsymbol{T}})\boldsymbol{W} = \boldsymbol{T}^p_h. \end{aligned}\right\} \tag{5.20}$$

The additional terms in (5.20) only strengthen the negative-definiteness of the grand lubrication resistance matrix in (5.10)–(5.11). Equations (5.20) are solved for

https://doi.org/10.1017/jfm.2014.15 Published online by Cambridge University Press

$\boldsymbol{W} = (\boldsymbol{V}^{agg}, \boldsymbol{\Omega}^{agg}, \boldsymbol{V}^{p}, \boldsymbol{\Omega}^{p})$ and the results are substituted into (5.19) and then into (5.18) to form the residuals for generalized minimal residual (GMRES) iterations. However, since Lamb's coefficients enter the equations in a very asymmetric way, it is desirable to have, at least, a motivated definition for the norm $\| \dots \|$ (and the related scalar product) in the solution space $\{A^{\alpha}_{-(\nu+1),m}, B^{\alpha}_{-(\nu+1),m}, C^{\alpha}_{-(\nu+1),m}\}$ required by GMRES (see appendix C).

5.3. *Economical truncation*

In addition to azimuthal truncation $|m'| \leqslant O(1)$, truncations in the multipole orders ν and n in Lamb's series (5.13) and (5.16) must also be made. For isolated rigid-body multiparticle clusters prepared by Monte Carlo methods, very accurate solutions are achieved (Filippov 2000) with low-order multipoles, owing to the absence of lubrication effects. In contrast, for a cluster closely interacting with a primary particle, we found it necessary to incorporate high-order multipoles, even after the geometry perturbation. In the iterative solution, it would be very wasteful to assign the same high truncation level $L \geqslant n, \nu$ to all Lamb's series (5.13) and (5.16), and to all re-expansions $\boldsymbol{u}^{\beta}_{-} \to \boldsymbol{u}^{\alpha}_{+}$. A better method must take into account that only close surfaces S_α and S_β may require high truncation levels $\nu^*(\alpha, \beta) \geqslant \nu$ and $n^*(\alpha, \beta) \geqslant n$ in the series (5.13) and (5.16), respectively, for the $\boldsymbol{u}^{\beta}_{-} \to \boldsymbol{u}^{\alpha}_{+}$ re-expansion. Elaborate strategies called 'economical truncation' were developed for multiparticle thermal interaction of spheres (Zinchenko 1994) and for multipole-accelerated boundary-integral calculations with many deformable drops (Zinchenko & Davis 2000, 2002, 2008). These techniques hinge upon plausible estimations of the rate of decrease of multipole coefficients, as $\nu, n \to \infty$, and result in a broad spectrum of truncation bounds ν^* and n^* strongly sensitive to the system geometry. The truncation rules here are much simpler and more intuitive, but they still use rigorous progression exponents for the rate of decay of multipole coefficients from binary interactions.

First, a sufficiently large truncation order k_o is set to limit n and ν in Lamb's series re-expansions between the cluster particles in contact when they are both far away from the primary particle S_{N+1}. The associated truncation error $\delta(k_o)$ is then estimated. For all other pairs S_α, S_β, the truncation bounds $\nu^*(\alpha, \beta)$ and $n^*(\alpha, \beta)$ on $\boldsymbol{u}^{\beta}_{-} \to \boldsymbol{u}^{\alpha}_{+}$ re-expansion are constructed in an economical manner to make the associated truncation errors compatible with δ. In particular, close proximity of the primary particle S_{N+1} to a cluster particle S_α requires much higher truncation levels than k_o in the $S_\alpha \leftrightarrow S_{N+1}$ re-expansions, but also tightens the truncation bounds for $S_\alpha \leftrightarrow S_\beta$ re-expansion between S_α and its near-neighbours S_β in the cluster somewhat above k_o. On the other hand, $\nu^*(\alpha, \beta) \ll k_o$ and $n^*(\alpha, \beta) \ll k_o$ for cluster particles S_α and S_β well separated from each other and from the primary particle. For a complete description of our truncation scheme, see appendix D. Although this truncation scheme is inevitably semi-intuitive, it depends on a single parameter k_o, and all multipoles are eventually included as $k_o \to \infty$, which guarantees convergence to the exact solution. This convergence is achieved much more efficiently than with the simplest uniform truncation level $L \geqslant \nu, n$ at $L \to \infty$. For very close particle–cluster interactions, the order of multipoles on the primary particle and in the vicinity reached 103 in our systematic runs of § 8 with $k_o = 11$. However, the code remains fast even in these conditions, due to the iterative solution and the economical re-expansion algorithm with azimuthal truncation.

The hydrodynamical algorithm for an isolated aggregate is just a simplification of the above scheme, with no need for geometry perturbation, and force/torque balance modification. Economical truncation also simplifies in the absence of the primary particle.

https://doi.org/10.1017/jfm.2014.15 Published online by Cambridge University Press

6. Miscellaneous details of the methodology

The dynamics (3.3) of an isolated N-particle cluster was integrated by the fourth-order Runge–Kutta (RK) scheme with the time step $\Delta t = 0.75a/V^{st}$, based on the steady-state speed V^{st} for the previous cluster with $N-1$ particles. The same scheme with $\Delta t = 0.3a/V^{st}$ was used to integrate particle–cluster relative trajectories, as long as the minimum particle–cluster surface clearance $\varepsilon_{min}a$ exceeds $0.05a$. For $0.01 < \varepsilon_{min} < 0.05$, the second-order RK scheme was used with $\Delta t = 0.03a/V^{st}$. In near-contact ($\varepsilon_{min} < 0.01$), we switched to the simplest Euler integration with $\Delta t = 0.003a/V^{st}$. In the range of substantial van der Waals attraction ($F_{vdW} \geqslant F^S$), further time-step reduction by a factor of $(F^S/F_{vdW})^{1/2}$ was found to be useful to avoid occasional stalling due to a large number of iterations. In near-contact, switching to low-order integration with small Δt was certainly more economical than using the fourth-order RK with the initial time step, but we did not try to optimize the time-step choices. For dominant van der Waals attraction ($F_{vdW} > 10F^S$), further time marching was unnecessary, and the primary particle was simply moved towards the nearest cluster particle to make $\varepsilon_{min} = 10^{-4}$, regarded as 'contact'. This tolerance is small enough not to affect the results. Still, the code is robust for even much smaller ε_{min}.

The speed of integrating particle–cluster relative trajectories also greatly benefits from careful construction of the initial approximation to the iterative solution $\boldsymbol{X} = \{A^{\alpha}_{-(\nu+1),m}, B^{\alpha}_{-(\nu+1),m}, C^{\alpha}_{-(\nu+1),m}\}$ of the hydrodynamical problem. For example, in the fourth-order RK, the system advancement to $t + \Delta t$ requires the Stokes flow solution at t, two predictor solutions at $t + \Delta t/2$, and one predictor solution at $t + \Delta t$. In each case, we start from $\boldsymbol{X}$ already computed at the given time, or use a linear extrapolation from two closest preceding time moments as the initial approximation. So, more than a few iterations were rarely needed.

7. Testing

In all the simulations below, lengths are scaled with the primary particle radius a; the linear velocity scale is the isolated sphere velocity U^S; rotational velocities are scaled with U^S/a; and time is scaled with a/U^S. Figure 6 shows fragments from the early stage of our cluster growth process, with moderate van der Waals attraction $\varepsilon_{vdW} = 0.005$ (§ 1). For an aggregate of five spheres in steady rotation (figure 6*a*), 52 random initial positions for a new primary particle were generated far below the aggregate, until a colliding trajectory was found (figure 6*b*,*c*,*d*). At $t = 114$, when the particle–cluster surface clearance ε_{min} is ≈ 0.047, the simulation was interrupted to compare our instantaneous velocities $\boldsymbol{W} = (\boldsymbol{V}^{agg}, \boldsymbol{\Omega}^{agg}, \boldsymbol{V}^{p}, \boldsymbol{\Omega}^{p})$, for the aggregate and the particle, with those provided by the simplest alternative code at the same configuration and the same external forces and torques (5.3)–(5.4). As the alternative, the boundary-integral (BI) solution was constructed, with unstructured surface triangulations and quadratic convergence in the number $N_{\triangle}$ of triangular elements per surface. The details of this BI test are given in appendix E, including the primary and cluster particle coordinates for reproducibility purposes. This simplest BI solution is uncompetitively slow, but it was possible to use it as a test only, with very fine triangulations, for the small system size. The comparison of the velocity components (1–3, top to bottom) between the two solutions is shown in table 1. Our converged solution at $k_o = 11$ and 21 is practically indistinguishable from the converged BI solution at $N_{\triangle} = 15\,360$. Increasing the azimuthal truncation from $m_{max} = 6$ to $m_{max} = 12$ in our solution does not have any effect on the results in table 1 within the accuracy shown. The clearance $\varepsilon_{min} \approx 0.047$ is still far from

https://doi.org/10.1017/jfm.2014.15 Published online by Cambridge University Press

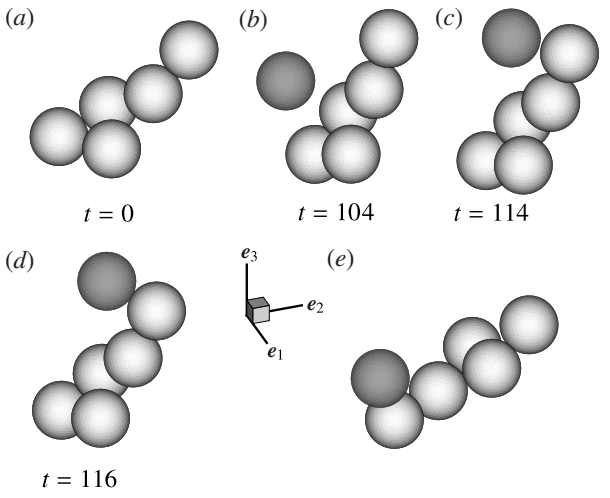


FIGURE 6. Snapshots from the early stage of the cluster growth process: (*a*) a five-sphere cluster in steady sedimentation (a new primary particle randomly generated far below it is not shown); (*b–d*) collision of the primary particle (dark shading) with the cluster; (e) a steady sedimentation regime for the new, six-sphere cluster (the cluster configuration is defined to within an arbitrary rotation about the vertical axis). The Cartesian axes orientation is the same for all frames.

the range where our method employs geometry perturbation (see below), so $\widehat{a} = a$ for table 1. It should be stressed again that k_o is only the series truncation level for cluster particles in contact but away from the primary particle, and our method attains exceptional accuracy through the efficient use of higher-order terms, when necessary (§ 5.3). For figure 6(*c*) and table 1 at $k_o = 11$, the primary particle interaction with the nearest cluster particle includes n and ν up to 42. The near-neighbour of the primary particle interacts with other cluster particles through the $\nu \leqslant 16$ (or $n \leqslant 16$) truncation. On the other hand, for the interaction between the cluster particles, which are away from each other and from the primary particle, $\max(\nu, n)$ in the re-expansion can be as low as 4.

For the simulation from figure 6(*a–d*) with $k_o = 11$ and $q_{max} = 0.9$, the dynamics of the particle–cluster surface clearance $\varepsilon_{min}(t)$ and of the particle centre vertical position $\Delta z(t)$ relative to the cluster centre $\boldsymbol{O}_g$ are presented in figure 7(*a*,*b*), respectively, by solid lines. The initial stages, with the particle and cluster widely separated, are not shown. At $t = 115.7$ ($\varepsilon_{min} = 0.01$), the progression exponent q for convergence of the primary particle interaction with the nearest cluster particle reaches q_{max}, which has necessitated multipoles of order 103 for this interaction. From this time moment, the geometry perturbation (§ 5.1) is gradually turned on, allowing the simulation to be continued to arbitrarily small separations without any further increase in the order of multipoles required. The whole dynamical simulation from $t = 0$ (with $\Delta z = -107$) to the particle–cluster collision required 4200 Stokes flow solutions (including 1100 solutions for strong particle–cluster interaction $t \geqslant 100$) and 35 s on a 3.6 GHz PC core. The run was repeated without the geometry perturbation ($q_{max} = 1$), not nearly as efficiently (5 min of CPU time), requiring multipoles of order 285 at the end of the simulation. The results, though, are indistinguishable from those shown by the solid lines in figure 7(*a*,*b*) (for example, the ultimate Δz at the contact is affected

https://doi.org/10.1017/jfm.2014.15 Published online by Cambridge University Press

	Boundary integral		Present solution		
	$N_\triangle = 3840$	$N_\triangle = 15360$	$k_o = 6$	$k_o = 11$	$k_o = 21$
$\boldsymbol{V}^{agg}$	−0.07775	−0.07799	−0.07794	−0.07800	−0.07799
	−0.13556	−0.13606	−0.13592	−0.13606	−0.13606
	−2.76637	−2.76644	−2.76637	−2.76646	−2.76644
$\boldsymbol{\Omega}^{agg}$	−0.02724	−0.02696	−0.02711	−0.02696	−0.02696
	0.01432	0.01424	0.01423	0.01423	0.01424
	−0.00226	−0.00222	−0.00231	−0.00222	−0.00222
$\boldsymbol{V}^{p}$	−0.00740	−0.00665	−0.00684	−0.00655	−0.00665
	0.01834	0.02015	0.01962	0.02013	0.02015
	−2.58378	−2.58394	−2.58399	−2.58392	−2.58395
$\boldsymbol{\Omega}^{p}$	−0.16675	−0.16665	−0.16638	−0.16671	−0.16666
	0.07657	0.07655	0.07642	0.07658	0.07655
	−0.00228	−0.00220	−0.00217	−0.00220	−0.00220

TABLE 1. Comparison of the present and boundary-integral solutions for the particle–cluster configuration from figure 6(*c*).

by 0.03 %). So, geometry perturbation is a practically seamless, efficient and accurate method to include lubrication. Another run with $k_o = 21$ and $q_{max} = 0.9$ was also made from the same initial condition, only to give $\varepsilon_{min}(t)$ and $\Delta z(t)$ graphically indistinguishable from those for $k_o = 11$ and $q_{max} = 0.9$; the effect on Δz at the collision is 0.3 %. This analysis, together with table 1, confirms the correctness and high accuracy of our results in figure 7.

Our method relies on very high-order multipoles, when necessary, and seeks to incorporate them most efficiently in dynamical simulations. In contrast, an alternative and well-known approach, which comes from Stokesian Dynamics (SD; Durlofsky, Brady & Bossis 1987) seeks a uniformly valid approximation to the solution of multiparticle problems by using relatively low-order multipoles only, combined with exact two-body solutions. A natural question is if the present, possibly more complex approach, is warranted for the problem considered herein. For comparison with our results in figure 7, we implemented the free-space SD version for the kinematic conditions specific for the cluster–particle pair. The instantaneous grand velocity vector $\boldsymbol{W}$ is calculated through the given grand force vector $\mathscr{F}$ as

$$\boldsymbol{W} = (\boldsymbol{M}_\infty^{-1} + \boldsymbol{R}_{2B} - \boldsymbol{R}_{2B}^{\infty})^{-1}\mathscr{F}, \quad \mathscr{F} = (\boldsymbol{F}_h^{agg}, \boldsymbol{T}_h^{agg}, \boldsymbol{F}_h^{p}, \boldsymbol{T}_h^{p}). \tag{7.1}$$

Here, $\boldsymbol{M}_\infty$ is the 12×12 far-field multibody mobility matrix, obtained from 12 multipole solutions for the cluster–particle pair, with uniform truncation level $L \geqslant \nu, n$ for all Lamb's series (5.13), (5.16) and all re-expansions. We still prefer the formalism of Lamb's singular solutions to facilitate using higher-order multipoles than is customary in SD. The 12×12 resistance matrix $\boldsymbol{R}_{2B}$ is defined so that $\boldsymbol{R}_{2B}\boldsymbol{W}$ is the total contribution to $\mathscr{F}$ from all pairwise interactions between the primary particle and cluster particles. To compute $\boldsymbol{R}_{2B}$, we decompose the translational/rotational velocities of the particles in each pair (prescribed by $\boldsymbol{W}$) into components along/normal to the line of centres and use the well-known exact two-body bispherical coordinate solutions in each case. Care is taken to eventually move the hydrodynamical torques on a cluster

https://doi.org/10.1017/jfm.2014.15 Published online by Cambridge University Press

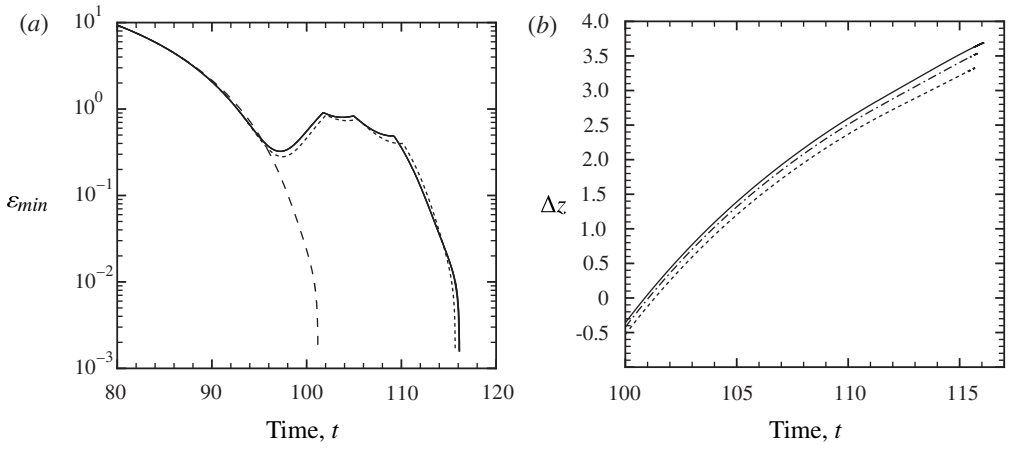


FIGURE 7. Dynamics (solid lines) of the non-dimensional (*a*) particle–cluster surface clearance and (*b*) particle vertical offset relative to the cluster centre for the simulation from figure 6(*a–d*). The long-dashed (in panel *a* only), short-dashed and dash-dotted lines are for the approximate solution using (7.1) from the same initial conditions, at $L = 6$, 8 and 9, respectively.

particle to the aggregate centre $\boldsymbol{O}_g$. The elements of $\boldsymbol{R}_{2B}$ are expressed in terms of several two-body scalar hydrodynamical functions (for the motion along/normal to the line-of-centres, etc.). The simplest way to calculate the far-field approximation $\boldsymbol{R}_{2B}^{\infty}$ to $\boldsymbol{R}_{2B}$ (which must be subtracted, in order not to count the same interactions twice (Durlofsky *et al.* 1987)) is to use the same algebra as for $\boldsymbol{R}_{2B}$, just replacing the exact two-body hydrodynamical functions with their far-field approximations. These approximations are obtained from the solutions of two-body mobility problems, with exactly the same multipole truncation $L \geqslant n, \nu$ as for $\boldsymbol{M}_{\infty}$, followed by inversion. Harshe *et al.* (2010), in their SD study of isolated multiparticle clusters (prepared by a Monte Carlo method), found that including two-body interactions between cluster particles in $\boldsymbol{R}_{2B} - \boldsymbol{R}_{2B}^{\infty}$ is not helpful and may even be deleterious, leading to large errors in the total drag force, especially for large N. Accordingly, our $\boldsymbol{R}_{2B} - \boldsymbol{R}_{2B}^{\infty}$ in (7.1) does not include such contributions.

To verify that our implementation of (7.1) is free from errors, we checked that: (i) in the absence of $\boldsymbol{R}_{2B} - \boldsymbol{R}_{2B}^{\infty}$, the result $\boldsymbol{W}$ is always identical to that by our code in § 5 at $\widehat{a} = a$, if the economical truncation therein is replaced by uniform truncation $L \geqslant \nu, n$ for all the series and re-expansions; (ii) for arbitrary $\boldsymbol{W}$ and the particle near the cluster, the contribution to $\boldsymbol{R}_{2B}\boldsymbol{W}$ from each pair is identical to that provided by high-resolution BI solution for the pair without decomposing $\boldsymbol{W}$ into particular motions along/normal to the line-of-centres; and (iii) all elements of $\boldsymbol{R}_{2B} - \boldsymbol{R}_{2B}^{\infty}$ disappear as the primary particle is separated from the cluster, all decaying more rapidly with distance as L increases. For the same initial conditions, the results of dynamical simulation based on (7.1) are shown in figure 7(*a*,*b*) by dashed and dash-dotted lines for different L. The $L = 4$ approximation (not shown) includes forces, torques and stresslets (a customary SD set) in the series (5.13), but was quite unsuccessful, showing separation after reaching $\varepsilon_{min} \approx 0.9$ instead of collision. The $L = 6$ approximation was still unacceptable, especially for $\Delta z(t)$ (outside the range of figure 7*b* to be shown). For $L = 8$, the approximation (7.1)

https://doi.org/10.1017/jfm.2014.15 Published online by Cambridge University Press

is reasonably good for $\varepsilon_{min}(t)$, but crude for $\Delta z(t)$, with an error of 10 % at the collision (such appreciable errors in determining the primary particle attachment position should affect the cluster growth process). With $L = 9$, this error decreases to 4 %. These deficiencies of the low-L approximations (7.1) were typical in our many tests for clusters of $N = 5$ spheres interacting with a primary particle. Interestingly, the $L = 4$ approximation (7.1) behaves much better for $N = 2$ in similar tests than for $N = 5$, so increasing the cluster size mandates higher-order multipoles in (7.1), which is a burden on the conventional SD and has required a different approach here. Obviously, the present problem behaves differently from those usually considered in SD applications. Although the low-L approximation (7.1) is seen to produce inaccurate system trajectories, it was not possible in the present work to explore the effect of these inaccuracies on the statistics of the cluster growth because of the very slow performance of the algorithm based on (7.1), even for $L = 4$. Accelerated SD algorithms (Guckel 1999; Sierou & Brady 2001; Meng & Higdon 2008; Kumar & Higdon 2011) are much faster than the conventional SD in many problems. These newer approaches, though, are substantially based on periodic boundaries (imperative for stable concentrated suspensions, but not relevant in the present problem) through the use of the particle-mesh-Ewald scheme and Fast Fourier Transform, and still do not address the issue of high-order multipoles.

The accuracy of the present code for particle–cluster interactions does not suffer appreciably with increasing the system size and/or reducing the strength of the van der Waals attraction. The solid lines in figure 8 show a fragment from a cluster growth realization for $k_o = 11$, $q_{max} = 0.9$ and weak attraction $\varepsilon_{vdW} = 0.00125$. The values of $\varepsilon_{min}(t)$ and $\Delta z(t)$ are for a colliding trajectory (found by trial and error) of a particle interacting with a cluster of $N = 49$ spheres. The whole trajectory from $t = 0$ (far below the cluster, not shown) to collision required 8000 Stokes flow solutions and 12 min of CPU time (suggesting approximately a linear scaling with N, at least for $N \leqslant O(10^2)$; see the $N = 5$ results). Again, the geometry perturbation is turned on at $\varepsilon_{min} \approx 0.01$, with the maximum order of multipoles reaching 103. Repeating the $k_o = 11$ run without perturbation ($q_{max} = 1$) required multipoles of order 590 at the end, but gave indistinguishable results for $\varepsilon_{min}(t)$ and $\Delta z(t)$ (the effect on Δz at the collision being 0.25 %). Finally, the difference between the runs $k_o = 21$, $q_{max} = 0.9$ (dashed lines) and $k_o = 11$, $q_{max} = 0.9$ (solid lines) is barely noticeable for $\varepsilon_{min}(t)$ and negligible for Δz (being 0.5 % at the collision). The grand velocity vector $\boldsymbol{W}$ is even more accurate.

Once the primary particle makes contact with the cluster, the next step (§ 3) is to determine the mobility tensors $\boldsymbol{M}_{\boldsymbol{\Omega F}}$ and $\boldsymbol{M}_{\boldsymbol{VF}}$ for the whole new aggregate through the solution of three Stokes flow problems for general description of the translational ($\boldsymbol{V}$) and rotational ($\boldsymbol{\Omega}$) cluster velocities. As a test, for the newly made cluster of six spheres in figure 6(*d*), we compared, in table 2, the initial velocities $\boldsymbol{V}$ and $\boldsymbol{\Omega}$ from our solution with those from the BI method (appendix C). Again, excellent agreement is seen between the two methods upon convergence ($N_\triangle = 8640$, $k_o = 11$); as expected, the case of an isolated cluster is handled accurately with low-order multipoles. For this aggregate, the mobility tensor $\boldsymbol{M}_{\boldsymbol{\Omega F}}$ has only one real eigenvalue, so the steady-state settling speed V^{st}, rotational velocity Ω^{st} and the radius R_{SR} of steady rotation can be predicted from (3.6), (3.5) and (3.8), respectively, without time integration. These values in table 2 are also weakly sensitive to the truncation parameter k_o; $R_{SR} = 13.2$ gives another example when the steady rotation radius greatly exceeds the hydrodynamical radius $R_h = 2.48$. The initial aggregate velocities $\boldsymbol{V}$ and $\boldsymbol{\Omega}$ in table 2 are quite different from steady-state $\boldsymbol{V} = (0, 0, -V^{st})$ and $\boldsymbol{\Omega} = (0, 0, \Omega^{st})$.

https://doi.org/10.1017/jfm.2014.15 Published online by Cambridge University Press

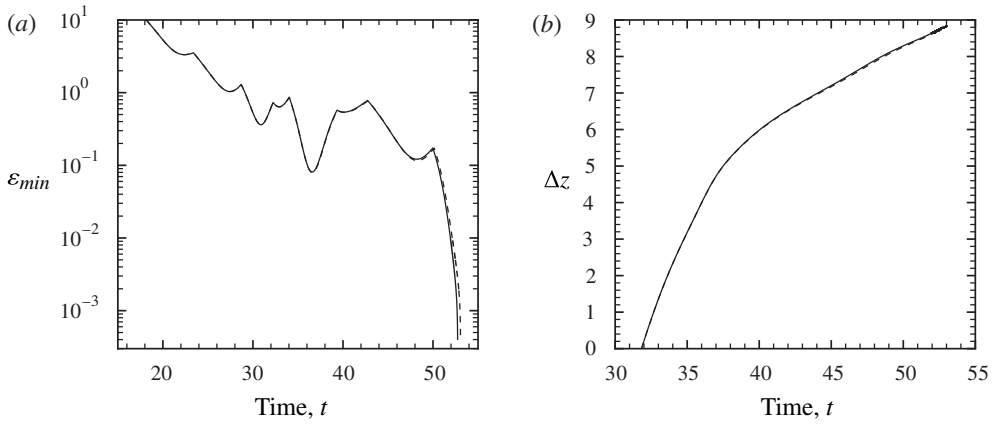


FIGURE 8. Dynamics of the non-dimensional (*a*) particle–cluster surface clearance and (*b*) particle vertical offset relative to the cluster centre for a particle collision with a cluster of $N = 49$ spheres; weak van der Waals attraction $\varepsilon_{vdW} = 0.00125$. The cluster hydrodynamical radius is $R_h = 6.27$. Lines: solid, $k_o = 11$, $q_{max} = 0.9$; dashed, $k_o = 21$, $q_{max} = 0.9$, starting from the same initial conditions.

	Boundary integral		Present solution	
	$N_\triangle = 3840$	$N_\triangle = 8640$	$k_o = 6$	$k_o = 11$
$\boldsymbol{V}$	−0.06262	−0.06262	−0.06261	−0.06262
	−0.11242	−0.11243	−0.11245	−0.11243
	−2.69814	−2.69810	−2.69819	−2.69811
$\boldsymbol{\Omega}$	−0.04623	−0.04623	−0.04625	−0.04623
	0.02069	0.02069	0.02069	0.02069
	−0.00400	−0.00400	−0.00403	−0.00400
V^{st}	—	—	2.42111	2.42108
Ω^{st}	—	—	0.00522	0.00523
R_{SR}	—	—	13.26721	13.23530

TABLE 2. Comparison of the present and the boundary-integral solutions for the six-particle cluster from figure 6(*d*). In addition to the cluster velocities $\boldsymbol{V}$ and $\boldsymbol{\Omega}$ for this configuration, the steady-state sedimentation speed V^{st}, rotational velocity Ω^{st} and the steady rotation radius R_{SR} for the aggregate are also given.

Dynamical integration (3.3) shows that $-V_3(t)$ and $\Omega_3(t)$ approach their steady-state values V^{st} and Ω^{st} in $t \sim 100$, with Ω_3 changing sign (figure 9); other components $V_i(t)$ and $\Omega_i(t)$ asymptote to zero. The vertical position Δz of the new cluster particle (relative to the new cluster centre $\boldsymbol{O}_g$) also undergoes a significant change, from 3.08 at collision (figure 6*d*) to the steady-state value of 0.75 (figure 6*e*).

As another test, for isolated multiparticle clusters of regular shapes in translational motion, the drag force from tables in Filippov (2000) was found to be in excellent agreement with our calculations. Our tables 1 and 2, though, provide more comprehensive testing for random arrangements.

https://doi.org/10.1017/jfm.2014.15 Published online by Cambridge University Press

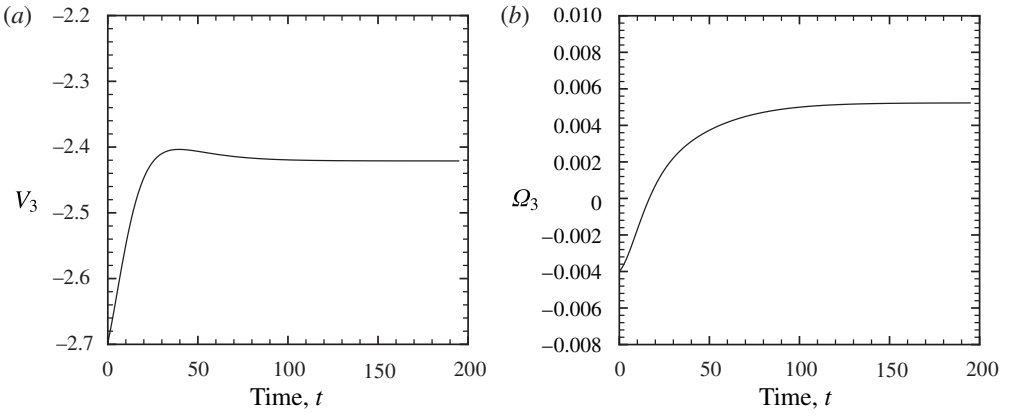


FIGURE 9. Evolution of (*a*) the sedimentational and (*b*) rotational velocities for the cluster from figure 6(*d*), as the steady sedimentation regime (figure 6*e*) is approached.

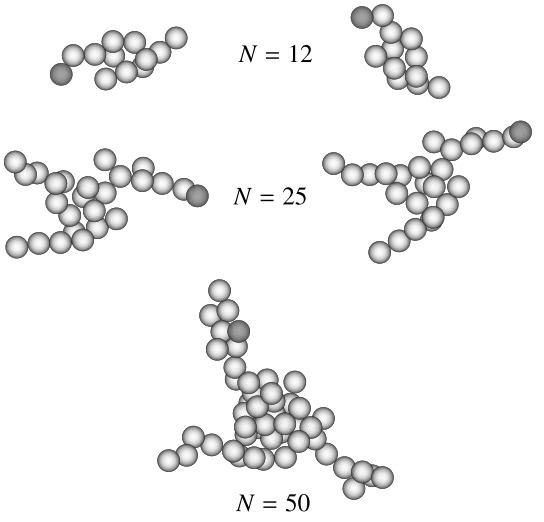


FIGURE 10. Examples of multiparticle clusters built in one realization of the growth process with weak van der Waals attraction $\varepsilon_{vdW} = 0.00125$. For $N = 12$ and 25, the left images are at the moment of a new particle attachment, and the right images (with the same view) are after reorientation to the steady sedimentation regime. For $N = 50$, only the moment of a new particle attachment is shown. The newly added particle is dark shaded. The clusters sediment downwards.

8. Hydrodynamical and statistical properties of large clusters

With the physical (ε_{vdW}) and accuracy ($k_o = 11$, $q_{max} = 0.9$) parameters preset, each realization of the cluster growth process is uniquely determined by the seed in the random number generator for initial particle positions far below the cluster. Figure 10 gives examples of clusters of $N = 12$, 25 and 50 spheres built in one realization with weak attraction $\varepsilon_{vdW} = 0.00125$. For $N = 12$ and 25, the left images are at the moment of a new particle attachment, and the right images are after the cluster reorientation to the state of steady rotation; the newly attached particle is shaded darker. There is

https://doi.org/10.1017/jfm.2014.15 Published online by Cambridge University Press

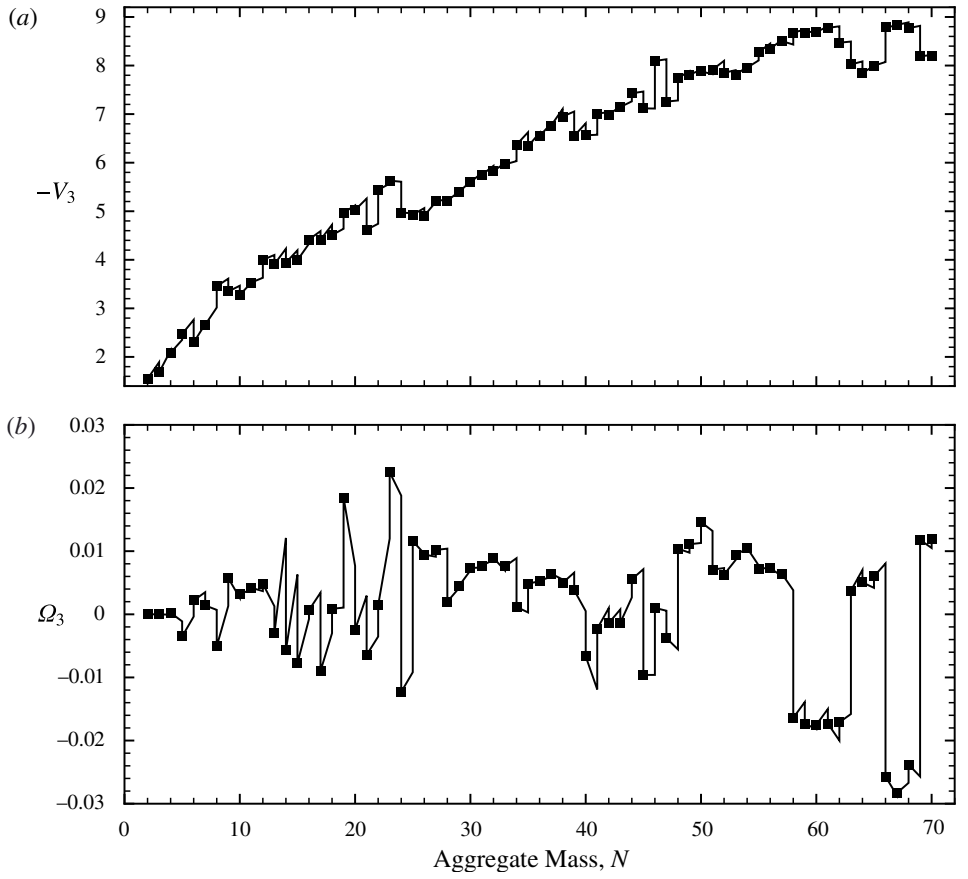


FIGURE 11. The non-dimensional (*a*) settling speed and (*b*) rotational velocity of the aggregates built in one growth realization with $\varepsilon_{vdW} = 0.00125$. For every N, unmarked values are for the moment of a new particle attachment; symbols are the steady-state values after the cluster equilibration.

quite significant vertical reorientation in both cases, even with the addition of just one particle. For $N = 50$, there is (accidentally) little change, and only the configuration at collision with the new particle is shown; this is the end point of the simulation from figure 8.

Figure 11a shows the vertical settling speed of the aggregates built in this realization versus the aggregate mass N. For every $N \geqslant 3$, we give two values: (i) when a new particle has just been added and (ii) after subsequent cluster equilibration to the steady state (marked with symbols). While adding a new particle generally works to increase the settling speed, the effect of subsequent cluster reorientation (represented by vertical jumps in figure 11*a*) may be of either sign and quite significant, even for large N. The vertical rotational velocity Ω_3 of the aggregates in this realization is shown in figure 11(*b*) in a similar manner. This velocity is small, but highly irregular, and can be of either sign. The average value of Ω_3 for every N is, of course, zero, but it can only be seen after ensemble averaging over many realizations.

For $\varepsilon_{vdW} = 0.02$ and 0.005, many growth realizations were generated to $N = 100$. Figure 12 shows the final steady-state aggregates from three different realizations with

https://doi.org/10.1017/jfm.2014.15 Published online by Cambridge University Press

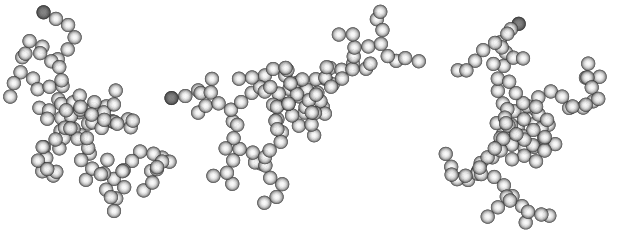


FIGURE 12. Steady-state aggregates of $N = 100$ spheres from three different growth realizations with $\varepsilon_{vdW} = 0.005$; the last attached primary particle is dark shaded. Horizontal view, sedimentation is downwards.

$\varepsilon_{vdW} = 0.005$. While for the leftmost aggregate the change of vertical orientation (since the last collision) to reach steady rotation was minimal, the other two aggregates in figure 12 required significant reorientation, with the last attached particle travelling a vertical distance about the aggregate centre comparable to the cluster size.

From the hydrodynamical viewpoint, it is most interesting to explore the ensemble-averaged aggregate settling speed, $\langle V^{st}\rangle$, versus the aggregate mass, N. This quantity $\langle V^{st}\rangle$ is shown in figure 13(a) for $\varepsilon_{vdW} = 0.02$ (dashed line), 0.005 (solid line) and 0.00125 (dash-dotted line), with averaging over 80 growth realizations in each case. To limit the computational effort, the $\varepsilon_{vdW} = 0.00125$ runs were terminated at $N = 70$. Figure 13(b) presents the standard deviation $\Delta = \sigma(V^{st})/\langle V^{st}\rangle$ of the settling speed relative to its average, versus N (for $\varepsilon_{vdW} = 0.02$ and 0.005 only). These results indicate statistical errors of 1.0–1.5 % with 95 % confidence in our values of $\langle V^{st}\rangle$ for large aggregates $N \sim 100$. Interestingly, the relative deviation Δ shows only a very mild downward trend as the cluster mass N increases. So, extensive ensemble averaging of the settling speed would still be imperative even for much larger clusters.

Figure 13(a) in log–log axes shows, though, that the present range $N \leqslant 70$–100 is sufficient to evaluate the fractal scaling $\langle V^{st}\rangle = \beta N^{\alpha}$ at $N \to \infty$. The best power fit to our data in figure 13(a) for $N \geqslant 25$ yields

$$\varepsilon_{vdW} = 0.02, \quad \langle V^{st}\rangle = 1.077N^{0.481}, \quad \langle\delta\rangle = 0.43\,\%, \quad \delta_{max} = 1.4\,\%, \quad (8.1a)$$

$$\varepsilon_{vdW} = 0.005, \quad \langle V^{st}\rangle = 1.131N^{0.477}, \quad \langle\delta\rangle = 0.44\,\%, \quad \delta_{max} = 1.6\,\%, \quad (8.1b)$$

$$\varepsilon_{vdW} = 0.00125, \quad \langle V^{st}\rangle = 1.184N^{0.475}, \quad \langle\delta\rangle = 0.40\,\%, \quad \delta_{max} = 1.2\,\%, \quad (8.1c)$$

with the corresponding average $\langle\delta\rangle$ and maximum δ_{max} relative errors; δ_{max} is consistent with the ensemble averaging error. These power fits are not shown in figure 13(a) because of their close proximity to the raw data for all $N \geqslant 25$. The exponent α is (practically) independent of the strength of the molecular force (provided that it remains short-range), while the prefactor β shows a 10 % variation between the cases of 'strong' and 'weak' van der Waals attraction. The accurate $N \gg 1$ approximations (8.1) are complemented by table 3 for small clusters $N \leqslant 25$. It is interesting to note, from both figure 13(a) and table 3, the kink of the data at $N = 3$, so that the log–log slope of $\langle V^{st}\rangle$ versus N is much different for small N than the ultimate value for large N.

With our non-dimensionalization (§ 7), the hydrodynamical radius R_h of a cluster of mass N is simply N/V^{st}. Additional geometrical quantities of interest are (i) the cluster height $H = z_{max} - z_{min}$, defined as the vertical distance between the highest and lowest points of the cluster surface, (ii) the outer radius R_{out}, defined as the maximum

https://doi.org/10.1017/jfm.2014.15 Published online by Cambridge University Press

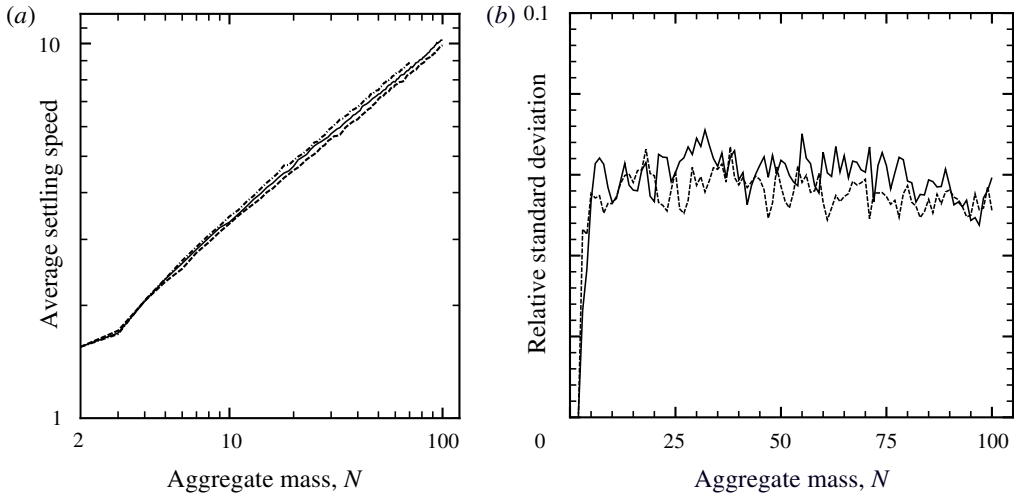


FIGURE 13. (*a*) The ensemble-averaged non-dimensional settling speed of the aggregates and (*b*) its relative standard deviation. Dashed line: strong molecular attraction $\varepsilon_{vdW} = 0.02$. Solid line: moderate attraction $\varepsilon_{vdW} = 0.005$. Dot-dashed line: weak attraction $\varepsilon_{vdW} = 0.00125$ (in panel (*a*) only). Each data point is obtained by averaging over 80 growth realizations.

ε_{vdW}	$N=2$	3	4	5	6	7	8	9
0.02	1.55	1.71	2.05	2.31	2.50	2.76	2.95	3.14
0.005	1.55	1.69	2.05	2.35	2.59	2.82	3.03	3.22
0.00125	1.55	1.68	2.06	2.35	2.63	2.87	3.08	3.26
ε_{vdW}	$N=10$	11	12	13	14	15	16	17
0.02	3.30	3.47	3.61	3.73	3.86	4.01	4.11	4.25
0.005	3.34	3.50	3.67	3.84	3.97	4.13	4.24	4.39
0.00125	3.45	3.59	3.78	3.92	4.10	4.26	4.39	4.53
ε_{vdW}	$N=18$	19	20	21	22	23	24	25
0.02	4.38	4.48	4.59	4.67	4.78	4.90	4.99	5.06
0.005	4.51	4.57	4.70	4.89	4.97	5.05	5.21	5.33
0.00125	4.73	4.74	4.87	4.99	5.07	5.18	5.29	5.44

TABLE 3. Ensemble-averaged settling speed of small aggregates $N \leqslant 25$.

distance from the aggregate centre of mass to the aggregate surface, (iii) the radius R_{pr} of the horizontal cluster projection (already defined in § 4 and figure 2), and (iv) the gyration radius

$$R_g = \left[1 + \frac{1}{N}\sum_{\alpha=1}^{N} r_\alpha^2\right]^{1/2}. \tag{8.2}$$

For the latter radius, most commonly employed to characterize the fractal geometry of multiparticle aggregates, we use the definition from Filippov (2000). The additional term in the brackets (8.2) (for particles of unit radius) serves to improve the behaviour of R_g at small N, although it may be neglected for $N \to \infty$. For moderate molecular

https://doi.org/10.1017/jfm.2014.15 Published online by Cambridge University Press

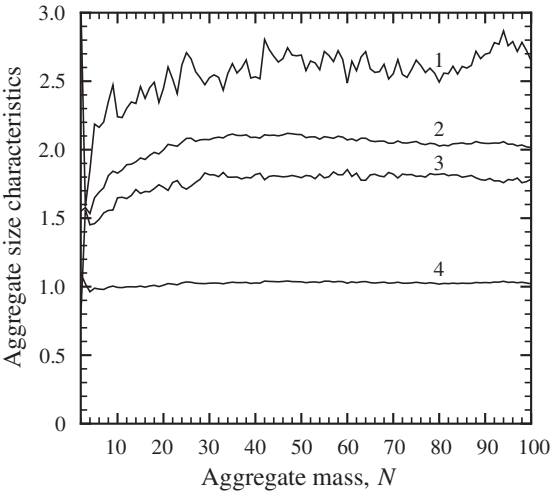


FIGURE 14. The aggregate size characteristics (averaged over 80 growth realizations) relative to the average hydrodynamical radius: height (1), outer radius (2), horizontal projection radius (3) and gyration radius (4), all for $\varepsilon_{vdW} = 0.005$.

attraction $\varepsilon_{vdW} = 0.005$, the ratios $\langle H\rangle/\langle R_h\rangle$, $\langle R_{out}\rangle/\langle R_h\rangle$, $\langle R_{pr}\rangle/\langle R_h\rangle$ and $\langle R_g\rangle/\langle R_h\rangle$ (curves 1–4, respectively) are shown in figure 14 versus the aggregate mass. The height H has the strongest statistical fluctuations, but R_{out} and R_{pr} are also more dispersed than R_g. For $N \gg 1$, on average, the outer radius is twice as large, and the projection radius is 1.8 times as large as the hydrodynamical radius. Remarkably, the average gyration radius is close to $\langle R_h\rangle$, within 4 %, for all $N \geqslant 3$. However, the relative standard deviations $\sigma(R_g)/\langle R_g\rangle$ for R_g are about twice as large as those for R_h, which makes it more difficult to completely eliminate statistical errors in $\langle R_g\rangle$ and accurately extract the usual fractal scaling $N \sim R_g^{d_f}$ from our simulations. Instead, the settling speed results (8.1) provide a more accurate power fit $N = k_h R_h^{d_f}$ at large N. For moderate attraction $\varepsilon_{vdW} = 0.005$, we have $d_f = 1.91$ with a prefactor $k_h = 1.27$. These parameters may be compared to $d_f = 1.93$, $k_h = 1.15$ at $\varepsilon_{vdW} = 0.02$, and $d_f = 1.90$, $k_h = 1.38$ at $\varepsilon_{vdW} = 0.00125$. Thus, with a small uncertainty, $d_f = 1.91 \pm 0.02$ is predicted as the only possible fractal dimension of rigid aggregates naturally formed in dilute sedimenting quiescent suspensions of non-Brownian monodisperse spheres with short-range molecular attractions. Our calculations also shed some light on the statistics of particle connectivity in such aggregates. From the analysis of the aggregates with $N = 100$ in 80 growth realizations at $\varepsilon_{vdW} = 0.005$, it is found that most particles are connected to one or two neighbours (33 % and 43 % of particles, respectively), although there are also particles with three or four neighbours (19 % and 5 %, respectively). Higher connectivities are statistically insignificant.

All our simulations discussed so far assumed vertical alignment of doublets (§ 2) as the initial condition for cluster growth. For comparison, table 4 gives the ensemble-averaged settling speed of small aggregates $N \leqslant 25$ for $\varepsilon_{vdW} = 0.005$ and a different initial condition, when the doublets are randomly oriented with uniform probability density. The statistical errors in table 4 are slightly larger than those in table 3, but still do not exceed 1.5 % with 95 % confidence for each N. Although it is unclear which physical mechanism could randomize the orientation for non-Brownian isolated

https://doi.org/10.1017/jfm.2014.15 Published online by Cambridge University Press

$N=2$	3	4	5	6	7	8	9	10	11	12	13
1.44	1.74	2.08	2.34	2.60	2.81	3.01	3.20	3.34	3.51	3.70	3.83
$N=14$	15	16	17	18	19	20	21	22	23	24	25
4.00	4.14	4.25	4.36	4.55	4.69	4.76	4.84	4.97	5.03	5.12	5.19

TABLE 4. Settling speed of small aggregates $N \leqslant 25$ from the simulations with random initial doublet orientation; averaging over 80 growth realizations, $\varepsilon_{vdW} = 0.005$. The exact value for $N=2$ is 1.437.

doublets, this alternative initial condition yields virtually the same average settling speed for all $N \geqslant 3$, to within statistical errors (see tables 4 and 3).

9. Comparison with experiments

From the analysis of various experimental data, the bounds 1.6–2.3 were obtained for the fractal dimension of multiparticle aggregates formed from differential sedimentation of non-Brownian particles (Jiang & Logan 1991; Logan & Kilps 1995). Our prediction $d_f = 1.91 \pm 0.02$ is in this range. For more detailed comparisons with the present theory, we could use only the settling speed data from Huang (1994) for flocs formed in a moderately polydisperse suspension by differential sedimentation. The mass contribution from primary particles with diameters 1–10 μm was 90 %, the median diameter being $2\bar{a} = 4.8$ μm. From the physical parameters in Huang (1994), the settling speed of a primary sphere of radius $\bar{a}$ is $U^S = 20.72$ μm s^{-1}. In our figure 15, the floc settling speed–flock diameter data from figure 1 of Huang (1994) are replotted in non-dimensional form, using $U^S = 20.72$ μm s^{-1} and $\bar{a} = 2.4$ μm as the velocity and length scales, respectively. There is clearly a sharp rise in the slope of data near $D = 110$ in figure 15, reflecting a much higher fractal dimension ($d_f \approx 3$) for large clusters compared to medium-sized ones. A likely explanation (cf. Huang 1994) is that large hydrodynamical stresses around a rapidly sedimenting cluster can break the balance of colloidal attractive and repulsive forces between cluster particles in the secondary minimum and rearrange them, so that such aggregates are no longer rigid. This possibility is ignored in the present theory with colloidal attractions only. Note also that the Reynolds number Re based on the physical floc settling speed and floc diameter is from 0.52 to 2 for the largest floc sizes (in the shaded area of figure 15), while $Re \leqslant 0.33$ for all other experimental points. This is another reason to exclude the shaded area from comparisons with the present theory based on the Stokes equations. Even for perfectly rigid aggregates, a universal fractal scaling in the whole range of Reynolds numbers should not be expected.

The floc diameters D in Huang (1994) were measured from images taken by a microscope–camera system with a horizontal axis, but the precise definition of D used in these experiments is unclear to us. The floc height H as D could be a convenient measure, since it is independent of an arbitrary floc rotation about the vertical axis in steady sedimentation. In contrast, the definitions $D = 2R_{out}$ or $D = 2R_{pr}$ appear irrelevant to the image analysis, especially for polydisperse flocs, since they are based on the location of the floc centre of mass. We assume here $D = H$, which is $\approx 2.6R_h$ as follows from figure 14 for $N \gg 1$. Using (8.1) and $R_h = N/V^{st}$, our predictions for the floc settling speed (scaled with the primary particle speed) versus the floc diameter (scaled with the primary particle radius) are $0.47D^{0.93}$, $0.53D^{0.91}$ and $0.58D^{0.90}$

https://doi.org/10.1017/jfm.2014.15 Published online by Cambridge University Press

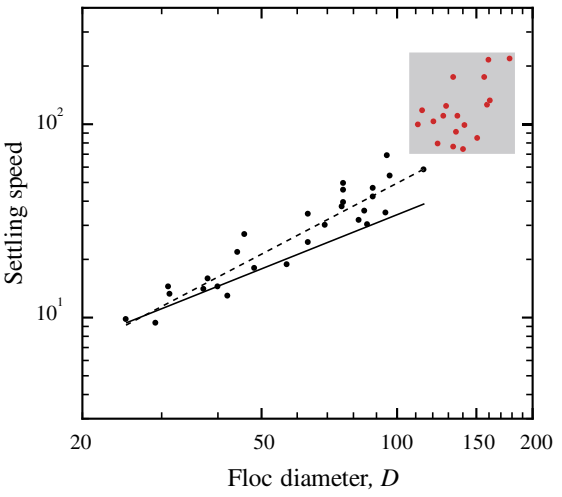


FIGURE 15. (Colour online) Non-dimensional settling speed of flocs formed in differential sedimentation as a function of the non-dimensional floc diameter. Symbols are experimental results from Huang (1994) for a moderately polydisperse suspension. Dashed line is the best power fit to the experimental points (excluding those in the shaded area). Solid line is from the present theory for monodisperse suspensions.

for $\varepsilon_{vdW} = 0.02$, 0.005 and 0.00125, respectively. For $a = 2.4$ μm and $\Delta\rho = 1.65$ g cm^{-3}, these values of ε_{vdW} correspond to the composite Hamaker constant $A_H = 1.1 \times 10^{-20}$ J, 7×10^{-22} J and 4×10^{-23} J, respectively. The solid line in figure 15 shows our prediction $0.47D^{0.93}$ for strong attraction $\varepsilon_{vdW} = 0.02$. The dashed line is the best power fit $0.18D^{1.22}$ to widely scattered experimental data (excluding the points in the shaded area). The agreement between the two lines is quite good in a wide range (the maximum deviation being 1.5 times at $D = 114$), considering the absence of adjustable parameters in our theory and inevitable effects of polydispersity, particle shape and surface charge in the experiments. Variation of ε_{vdW} has a very minor effect on the theoretical line in figure 15, much smaller than the scatter of the experimental points. Using $2R_{out}$ as the alternative definition of the floc diameter would clearly overpredict experimental measurements of D, but it would only reduce our theoretical floc speed by a factor of 1.5. Presumably, the assumption of the floc rigidity in our growth model is the main reason for the slight underestimation of the slope in figure 15 and the fractal dimension of flocs, compared to the experimental data of Huang (1994).

10. Concluding remarks

The present work offers the first rigorous and highly accurate hydrodynamical simulations of multiparticle aggregation in dilute sedimenting suspensions close to how it naturally originates. The primary particles are monodisperse spheres; Brownian and inertial effects are neglected. An N-particle rigid cluster captures a new primary particle (randomly generated far below the cluster), and the newly formed rigid cluster is allowed to reach steady sedimentation before a new particle is captured, etc. The growth process has to start from doublet–particle interaction, but the indeterminate doublet concentration has no effect on the statistics of generated clusters. Fast

https://doi.org/10.1017/jfm.2014.15 Published online by Cambridge University Press

aggregation conditions are assumed, with only attractive, short-range molecular forces present to overcome lubrication and form rigid clusters that do not rearrange (but do reorient) after capturing a new particle. In this problem, accurate simulation of cluster–particle relative trajectories for $N \gg 1$ requires a rigorous high-order multipole–multiparticle algorithm, rather than combining low-order expansions with exact two-body solutions. The present algorithm works very efficiently with such multipoles (to order 100, when necessary) through rotational transformations of spherical harmonics, economical truncation of multipole expansions/re-expansions and iterative solutions. In addition, the idea of geometry perturbation (adapted from multiparticle conductivity simulations of Zinchenko (1998)) extends the algorithm to arbitrarily small particle–cluster surface separations. Once a new particle is attached to the cluster, further cluster dynamics is predicted very efficiently, via tensor transformations and semi-analytical time integration. This part of the solution greatly benefits from free-space boundary conditions at infinity. The resulting steady sedimentation regime is spiral motion around the vertical 'axis of steady rotation'. Interestingly, this axis, found analytically from the solution of a new eigenvalue problem, is typically quite away from the aggregate centre of mass, at a distance much larger than the cluster size. A physically justified, yet efficient, strategy of generating new particle positions far below a cluster, with a uniform probability density (corresponding to homogeneous suspensions, prior to aggregation) is non-trivial due to cluster rotation and fractal-like shapes. An upper bound on the interception area is successfully found by backward integration of many cluster–particle relative trajectories from the cluster vicinity in the far-field approximation. Still, even in the optimized form, this strategy greatly overestimates the actual interception area. So, when a cluster size grows to $N \sim 100$, a large number of trial trajectories (in the exact hydrodynamical formulation) are typically required to obtain a new particle–cluster collision. This burden has limited the present simulations by $N \leqslant 100$. Generating a few larger clusters, though, would be far less important than extensive ensemble averaging over systems of moderate size, due to a large dispersion. For a typical 'moderate' van der Waals attraction, averaging over 80 growth realizations to $N = 100$ requires computing a total of 300 000 particle–cluster relative trajectories.

Upon such averaging, the aggregate settling speed V^{st}, relative to the primary particle speed, quickly attains a fractal scaling $V^{st} = \beta N^{\alpha}$, once $N \geqslant 25$. The exponent $\alpha \approx 0.48$ is practically independent of the molecular force strength, while the prefactor β shows a modest 10 % variation as the Hamakar constant varies in a broad range. As N grows, all average characteristics of the cluster size (in units of the particle radius) become proportional to the average hydrodynamical radius $R_h = N/V^{st}$: the outer radius $R_{out} \approx 2R_h$, the horizontal projection radius $R_{pr} \approx 1.8R_h$ and the cluster height $H \approx 2.6R_h$. Interestingly, the gyration radius R_g is close to R_h, within 4 %, for all $N \geqslant 3$. Of all these size characteristics, though, the hydrodynamical radius is by far the least subject to statistical errors and hence most suitable for calculating the cluster fractal dimension d_f from $N \sim R_h^{d_f}$. In this manner, our solution predicts, with a small uncertainty, $d_f = 1.91 \pm 0.02$ as the only possible value for rigid aggregates naturally formed in dilute sedimenting quiescent suspensions of non-Brownian monodisperse spheres with short-range molecular attractions. This result is consistent with the bounds 1.6–2.3 on d_f (Jiang & Logan 1991; Logan & Kilps 1995) from the analysis of various experimental data for aggregates formed in differential settling. A more detailed comparison of our solution with the experiments of Huang (1994) for the floc settling speed V^{st} versus floc diameter D shows a reasonably good quantitative agreement in a broad range of floc sizes, considering the absence of adjustable

https://doi.org/10.1017/jfm.2014.15 Published online by Cambridge University Press

parameters in our theory and inevitable effects of polydispersity, particle shape and some electrostatic repulsion in the experiments. The repulsion can add some flexibility to the aggregates, thus slightly increasing the slope of $\log V^{st}$ versus $\log D$, compared to our theory.

It is often stated (e.g. Sutherland 1966; Meakin 1985; Schaefer 1989; Logan & Wilkinson 1990; Vanni 2000) that cluster growth models with sequential particle addition, one at a time, can only produce aggregates of high fractal dimension $d_f = 2.5$–3.0 (rarely observed in experiments). Presumably for this reason, the focus in the literature has been on Monte Carlo growth models based instead on random cluster–cluster aggregation (DLCA–RLCA models, and the algorithm with tunable fractal dimension (Thouy & Jullien 1996)). These models, though, appear unjustified from the physical viewpoint even in the Brownian regime, and they are certainly irrelevant to cluster growth through differential settling. The present study conflicts with the existing views in that our rather low fractal dimension $d_f = 1.91 \pm 0.02$ is obtained from rigorous hydrodynamical simulations with sequential particle addition. There is no mathematical reason to expect a crossover from our solution to a different fractal regime at larger N, as long as our physical assumptions (aggregate rigidity, zero Reynolds number, infinite dilution) continue to hold. The physical reason for low fractal dimension obtained in our sequential-addition cluster growth simulations is that a cluster acts roughly as a sphere of a large hydrodynamical radius often preventing a new primary particle from reaching the cluster core. Even when d_f, a free parameter in Monte Carlo growth models, is close to our result 1.91 ± 0.02, the geometrical and hydrodynamical properties of the resulting clusters would still differ from those for our aggregates. For example, the radius R_s of the smallest sphere around a DLCA–RLCA cluster ($1.85 \leqslant d_f \leqslant 2.05$) is, on average, $\approx 1.65 R_g$ for $N \gg 1$ (Lattuada *et al.* 2003), while it is $1.9 R_g$ for our clusters. From the hydrodynamical drag force simulations of Binder *et al.* (2006, 2009) for DLCA-generated clusters with $d_f = 1.85$, the settling speed dependence $V^{st} \sim N^{0.37-0.38}$ is predicted, in contrast to our $V^{st} \sim N^{0.48}$. Obviously, d_f does not completely characterize random multiparticle clusters, and the underlying growth mechanism is important. In addition to different average size characteristics (see above), our solution gives information about particle connectivity in the clusters.

The present approach and techniques have the potential for future, more complex, rigorous hydrodynamical simulations of the statistics of cluster growth by single particle addition in polydisperse systems, and for flexible aggregates of solid particles or emulsion drops. The kinetics of cluster growth (not addressed in this work) is obviously a much harder problem but it can potentially be studied by combining the present technique with population dynamics. A difficult but necessary element is determining the average capture efficiency for each cluster size.

Acknowledgement

We are grateful to the anonymous reviewer for the critical suggestion to study the effect of the initial doublet orientation on the cluster growth.

Appendix A. Constructing the collision circle $\overline{S}_\infty$

Once a large number of end points $\boldsymbol{y}^1, \ldots, \boldsymbol{y}^M \in \pi_\infty$ of the trajectories (4.1) are obtained by backward integration (figure 3), we use a simple algorithm to construct a minimal circle $\overline{S}_\infty$ around these points, with sufficient accuracy and $O(M)$ cost. For any given $\alpha \in [0, \pi/2)$, it is easy to find a minimal rectangle in the plane π_∞, with

https://doi.org/10.1017/jfm.2014.15 Published online by Cambridge University Press

the sides along $(\cos\alpha, \sin\alpha, 0)$ and $(-\sin\alpha, \cos\alpha, 0)$, in the coordinate system of figure 3. Let $R_c(\alpha)$ be the maximum distance from $\boldsymbol{y}^j$ $(j=1,\ldots,M)$ to the rectangle centre. Minimization of $R_c(\alpha)$ (we use 20 test values of α) determines the radius and location of $\overline{S}_\infty$.

Appendix B. Lubrication matrices for geometry perturbation

Let h_α be the surface clearance between a cluster particle S_α and the primary particle S_{N+1} in the original geometry. After shrinking the radius of S_{N+1} to $\widehat{a}$ (figure 5), this gap increases to $\widehat{h}_\alpha$. For a close pair (S_α, S_{N+1}) moving with translational $(\boldsymbol{V}_\alpha, \boldsymbol{V}_{N+1})$ and rotational $(\boldsymbol{\Omega}_\alpha, \boldsymbol{\Omega}_{N+1})$ velocities, the well-known near-contact asymptotic solutions (Cooley & O'Neill 1969; O'Neill & Majumdar 1970) are used to write the hydrodynamical forces $\boldsymbol{F}_\alpha$ and $\boldsymbol{F}_{N+1}$ and torques $\boldsymbol{T}_\alpha$ and $\boldsymbol{T}_{N+1}$ (about the centres $\boldsymbol{x}^\alpha$ and $\boldsymbol{x}^{N+1}$) acting on S_α and S_{N+1}. The same solutions are employed to write these forces and torques (now denoted $\widehat{\boldsymbol{F}}_\alpha$, $\widehat{\boldsymbol{F}}_{N+1}$, ...) after the geometry perturbation (assuming the same kinematics $\boldsymbol{V}_\alpha$, $\boldsymbol{V}_{N+1}$, $\boldsymbol{\Omega}_\alpha$, $\boldsymbol{\Omega}_{N+1}$). One obtains

$$\begin{aligned}\boldsymbol{F}_\alpha - \widehat{\boldsymbol{F}}_\alpha \;=\; & \Psi_{\alpha,N+1}(\boldsymbol{V}_{N+1}-\boldsymbol{V}_\alpha)^{\parallel} + \Phi_{\alpha,N+1}(\boldsymbol{V}_{N+1}-\boldsymbol{V}_\alpha)^{\perp} \\ & + A_{\alpha,N+1}(\boldsymbol{n}_{\alpha,N+1}\times\boldsymbol{\Omega}_\alpha) + A_{N+1,\alpha}(\boldsymbol{n}_{\alpha,N+1}\times\boldsymbol{\Omega}_{N+1})\end{aligned} \tag{B 1}$$

and

$$\boldsymbol{T}_\alpha - \widehat{\boldsymbol{T}}_\alpha = A_{\alpha,N+1}\boldsymbol{n}_{\alpha,N+1}\times(\boldsymbol{V}_{N+1}-\boldsymbol{V}_\alpha) - C_{\alpha,N+1}\boldsymbol{\Omega}_\alpha^{\perp} - D_{\alpha,N+1}\boldsymbol{\Omega}_{N+1}^{\perp}. \tag{B 2}$$

Here, $\parallel$ and $\perp$ denote vector components along and normal to the line of centres $[\boldsymbol{x}^\alpha, \boldsymbol{x}^{N+1}]$, respectively; $\boldsymbol{n}_{\alpha,N+1}$ is the unit director of $\boldsymbol{x}^{N+1}-\boldsymbol{x}^\alpha$; and

$$\Psi_{\alpha,N+1} = 6\pi\left[\frac{a^2}{4h_\alpha} + \frac{9a}{40}L - \frac{(a\widehat{a})^2}{\widehat{h}_\alpha(a+\widehat{a})^2} - \frac{a\widehat{a}(a^2+7a\widehat{a}+\widehat{a}^2)}{5(a+\widehat{a})^3}\widehat{L}\right], \tag{B 3}$$

$$\Phi_{\alpha,N+1} = \frac{8\pi}{5}\left[\frac{5a}{8}L - \frac{a\widehat{a}(2a^2+a\widehat{a}+2\widehat{a}^2)}{(a+\widehat{a})^3}\widehat{L}\right], \tag{B 4}$$

$$A_{\alpha,N+1} = \frac{4}{5}\pi\left[\frac{5a^2}{4}L - \frac{a^2\widehat{a}(4a+\widehat{a})}{(a+\widehat{a})^2}\widehat{L}\right], \tag{B 5}$$

$$C_{\alpha,N+1} = \frac{16\pi}{5}\left[\frac{a^3}{2}L - \frac{a^3\widehat{a}}{(a+\widehat{a})}\widehat{L}\right], \tag{B 6}$$

$$D_{\alpha,N+1} = \frac{4\pi}{5}\left[\frac{a^3}{2}L - \frac{a^2\widehat{a}^2}{(a+\widehat{a})}\widehat{L}\right], \tag{B 7}$$

$$L = \ln\left(\frac{2a}{h_\alpha}\right), \quad \widehat{L} = \ln\left(\frac{a+\widehat{a}}{\widehat{h}_\alpha}\right). \tag{B 8}$$

The expression for $A_{N+1,\alpha}$ differs from (B 5) by interchanging a and $\widehat{a}$ in the subtracted term only. For $\boldsymbol{F}_{N+1}-\widehat{\boldsymbol{F}}_{N+1}$ and $\boldsymbol{T}_{N+1}-\widehat{\boldsymbol{T}}_{N+1}$, (B 1) and (B 2) apply with α and $N+1$ interchanged, $\boldsymbol{n}_{N+1,\alpha}=-\boldsymbol{n}_{\alpha,N+1}$, and Ψ, Φ and D coefficients unaffected. Again, $C_{N+1,\alpha}$ is obtained from (B 6) by interchanging a and $\widehat{a}$ in the subtracted term only.

It remains to substitute $\boldsymbol{V}_\alpha = \boldsymbol{V}^{agg} + \boldsymbol{\Omega}^{agg}\times\boldsymbol{r}_\alpha$, $\boldsymbol{\Omega}_\alpha = \boldsymbol{\Omega}^{agg}$, $\boldsymbol{V}_{N+1} = \boldsymbol{V}^p$ and $\boldsymbol{\Omega}_{N+1} = \boldsymbol{\Omega}^p$ into (B 1)–(B 2) and similar expressions for $\boldsymbol{F}_{N+1}-\widehat{\boldsymbol{F}}_{N+1}$ and $\boldsymbol{T}_{N+1}-\widehat{\boldsymbol{T}}_{N+1}$,

https://doi.org/10.1017/jfm.2014.15 Published online by Cambridge University Press

move the torques about $\boldsymbol{x}^\alpha$ to the cluster centre $\boldsymbol{O}_g$, and sum up all such singular contributions over lubrication pairs $(\alpha, N+1)$, $\alpha \in \mathscr{L}$ (typically, though, only one α contributes). The lubrication operators in (5.10)–(5.11) can be expanded as

$$\left.\begin{aligned}
(\boldsymbol{R}_{\boldsymbol{F}}^{agg} - \widehat{\boldsymbol{R}}_{\boldsymbol{F}}^{agg})\boldsymbol{W} &= \boldsymbol{F}_{\boldsymbol{V}}^{a,a}\boldsymbol{V}^{agg} + \boldsymbol{F}_{\boldsymbol{\Omega}}^{a,a}\boldsymbol{\Omega}^{agg} + \boldsymbol{F}_{\boldsymbol{V}}^{a,p}\boldsymbol{V}^{p} + \boldsymbol{F}_{\boldsymbol{\Omega}}^{a,p}\boldsymbol{\Omega}^{p},\\
(\boldsymbol{R}_{\boldsymbol{T}}^{agg} - \widehat{\boldsymbol{R}}_{\boldsymbol{T}}^{agg})\boldsymbol{W} &= \boldsymbol{T}_{\boldsymbol{V}}^{a,a}\boldsymbol{V}^{agg} + \boldsymbol{T}_{\boldsymbol{\Omega}}^{a,a}\boldsymbol{\Omega}^{agg} + \boldsymbol{T}_{\boldsymbol{V}}^{a,p}\boldsymbol{V}^{p} + \boldsymbol{T}_{\boldsymbol{\Omega}}^{a,p}\boldsymbol{\Omega}^{p},\\
(\boldsymbol{R}_{\boldsymbol{F}}^{p} - \widehat{\boldsymbol{R}}_{\boldsymbol{F}}^{p})\boldsymbol{W} &= \boldsymbol{F}_{\boldsymbol{V}}^{p,a}\boldsymbol{V}^{agg} + \boldsymbol{F}_{\boldsymbol{\Omega}}^{p,a}\boldsymbol{\Omega}^{agg} + \boldsymbol{F}_{\boldsymbol{V}}^{p,p}\boldsymbol{V}^{p} + \boldsymbol{F}_{\boldsymbol{\Omega}}^{p,p}\boldsymbol{\Omega}^{p},\\
(\boldsymbol{R}_{\boldsymbol{T}}^{p} - \widehat{\boldsymbol{R}}_{\boldsymbol{T}}^{p})\boldsymbol{W} &= \boldsymbol{T}_{\boldsymbol{V}}^{p,a}\boldsymbol{V}^{agg} + \boldsymbol{T}_{\boldsymbol{\Omega}}^{p,a}\boldsymbol{\Omega}^{agg} + \boldsymbol{T}_{\boldsymbol{V}}^{p,p}\boldsymbol{V}^{p} + \boldsymbol{T}_{\boldsymbol{\Omega}}^{p,p}\boldsymbol{\Omega}^{p}.
\end{aligned}\right\} \tag{B 9}$$

The independent 3×3 matrices on the right-hand side of (B 9) are given by

$$\left.\begin{aligned}
\boldsymbol{F}_{\boldsymbol{V}}^{a,a} &= -\sum[\Psi\boldsymbol{nn} + \Phi(\boldsymbol{I}-\boldsymbol{nn})],\\
\boldsymbol{F}_{\boldsymbol{\Omega}}^{a,a} &= \sum \Psi\boldsymbol{n}(\boldsymbol{n}\times\boldsymbol{r}) + \sum \Phi[\boldsymbol{R} - \boldsymbol{n}(\boldsymbol{n}\times\boldsymbol{r})] + \sum A_{\alpha,N+1}\boldsymbol{N},\\
\boldsymbol{F}_{\boldsymbol{\Omega}}^{a,p} &= \sum A_{N+1,\alpha}\boldsymbol{N},\\
\boldsymbol{T}_{\boldsymbol{\Omega}}^{a,a} &= \sum A_{\alpha,N+1}[\boldsymbol{rn} + \boldsymbol{nr} - 2(\boldsymbol{r}\cdot\boldsymbol{n})\boldsymbol{I}] - \sum C_{\alpha,N+1}(\boldsymbol{I}-\boldsymbol{nn})\\
&\quad - \sum \Psi(\boldsymbol{r}\times\boldsymbol{n})(\boldsymbol{r}\times\boldsymbol{n}) + \sum \Phi[\boldsymbol{rr} - r^2\boldsymbol{I} + (\boldsymbol{r}\times\boldsymbol{n})(\boldsymbol{r}\times\boldsymbol{n})],\\
\boldsymbol{T}_{\boldsymbol{\Omega}}^{a,p} &= -\sum D(\boldsymbol{I}-\boldsymbol{nn}) - \sum A_{N+1,\alpha}[(\boldsymbol{r}\cdot\boldsymbol{n})\boldsymbol{I} - \boldsymbol{nr}],\\
\boldsymbol{T}_{\boldsymbol{\Omega}}^{p,p} &= -\sum C_{N+1,\alpha}(\boldsymbol{I}-\boldsymbol{nn}).
\end{aligned}\right\} \tag{B 10}$$

Here, all the summations are over the lubrication set $\mathscr{L} \ni \alpha$ (defined in § 5.1) and, for brevity, $\Psi = \Psi_{\alpha,N+1}$, $\Phi = \Phi_{\alpha,N+1}$, $D = D_{\alpha,N+1}$, $\boldsymbol{n} = \boldsymbol{n}_{\alpha,N+1}$, $\boldsymbol{r} = \boldsymbol{r}_\alpha$,

$$\boldsymbol{N} = \begin{pmatrix} 0 & -n_3 & n_2\\ n_3 & 0 & -n_1\\ -n_2 & n_1 & 0 \end{pmatrix}, \quad \boldsymbol{R} = \begin{pmatrix} 0 & -r_3 & r_2\\ r_3 & 0 & -r_1\\ -r_2 & r_1 & 0 \end{pmatrix}. \tag{B 11}$$

Dyadics $\boldsymbol{ab}$ are defined as $(\boldsymbol{ab})_{ij} = a_i b_j$. The other matrices in (B 9) are simply

$$\left.\begin{aligned}
&\boldsymbol{F}_{\boldsymbol{V}}^{a,p} = \boldsymbol{F}_{\boldsymbol{V}}^{p,a} = -\boldsymbol{F}_{\boldsymbol{V}}^{p,p} = -\boldsymbol{F}_{\boldsymbol{V}}^{a,a},\\
&\boldsymbol{F}_{\boldsymbol{\Omega}}^{p,a} = -\boldsymbol{F}_{\boldsymbol{\Omega}}^{a,a}, \quad \boldsymbol{F}_{\boldsymbol{\Omega}}^{p,p} = -\boldsymbol{F}_{\boldsymbol{\Omega}}^{a,p},\\
&\boldsymbol{T}_{\boldsymbol{V}}^{a,a} = -\boldsymbol{T}_{\boldsymbol{V}}^{a,p} = (\boldsymbol{F}_{\boldsymbol{\Omega}}^{a,a})^*, \quad \boldsymbol{T}_{\boldsymbol{V}}^{p,a} = (\boldsymbol{F}_{\boldsymbol{\Omega}}^{a,p})^*,\\
&\boldsymbol{T}_{\boldsymbol{V}}^{p,p} = (\boldsymbol{F}_{\boldsymbol{\Omega}}^{p,p})^*, \quad \boldsymbol{T}_{\boldsymbol{\Omega}}^{p,a} = (\boldsymbol{T}_{\boldsymbol{\Omega}}^{a,p})^*,
\end{aligned}\right\} \tag{B 12}$$

where the asterisk is for the transpose.

Appendix C. The norm in the solution space for GMRES iterations

Instead of Lamb's multipole contribution (5.13) from a particle centre $\boldsymbol{x}^\beta$, stokeslets can be distributed over the surface S_β with some vector density $\boldsymbol{f}(\boldsymbol{x})$. It is natural to associate the norm $\|\ldots\|$ with the r.m.s. of $\boldsymbol{f}(\boldsymbol{x})$ over all surfaces S_β. Expanding $\boldsymbol{f}(\boldsymbol{x})$

https://doi.org/10.1017/jfm.2014.15 Published online by Cambridge University Press

in orthogonal vector harmonics (Schmitz & Felderhof 1982), the two representations can be related, yielding the rotationally invariant norm definition

$$\|\dots\|^2 = \sum_{\alpha=1}^{N+1} \int_{S_\alpha} \boldsymbol{f}^2(\boldsymbol{x})\,\mathrm{d}S = \sum_{\alpha=1}^{N+1} \sum_{\nu=1}^{\infty} Q_{\nu,\alpha}^2, \tag{C 1}$$

with

$$Q_{\nu,\alpha}^2 = \frac{a_\alpha^2(2\nu+1)}{\nu} \sum_{m=-\nu}^{\nu} |A^\alpha_{-(\nu+1),m}|^2 + \nu(\nu+1)(2\nu+1)^2 \sum_{m=-\nu}^{\nu} |C^\alpha_{-(\nu+1),m}|^2 + \frac{(2\nu+3)^2(\nu+1)(2\nu+1)}{\nu^2} \sum_{m=-\nu}^{\nu} \left| \frac{a_\alpha}{2} A^\alpha_{-(\nu+1),m} - \frac{(2\nu+1)}{a_\alpha} B^\alpha_{-(\nu+1),m} \right|^2. \tag{C 2}$$

Appendix D. Details of the economical truncation

As a prerequisite, a model problem for two spheres of unit radius moving as a rigid body under the action of unit forces (I) along and (II) normal to the centreline is solved by high-order expansions (5.13) in a wide range of centre separations $\zeta \geqslant 2$. The intensities (C 2) Q_ν^I and Q_ν^{II} are calculated in both cases, with $Q_\nu(\zeta) = \max(Q_\nu^I, Q_\nu^{II})$ defined to suppress oscillations in Q_ν^I and Q_ν^{II}. By definition, $Q_\nu = [q(\zeta)]^\nu Z_\nu$, where $q(\zeta) = [\zeta - (\zeta^2 - 4)^{1/2}]/2$ (see (5.5)), and $Z_\nu(\zeta)$ presumably of algebraic decay is tabulated. Near-contact simplification for q should not be made. This Q_ν models the decay of multipole coefficients for $\boldsymbol{u}_-^\beta \to \boldsymbol{u}_+^\alpha$ re-expansion between two particles in the cluster. It is also found that, for two spheres of unit radius moving along the centreline under the action of equal but opposite unit forces, the intensity (C 1) of the solution behaves roughly as $0.5n[q(\zeta)]^n$. So, we take $0.5n(\widehat{q}_\beta)^n$ as the model for the behaviour of the multipole coefficients on S_{N+1} in the $\boldsymbol{u}_-^\beta \to \boldsymbol{u}_+^{N+1}$ (or vice versa) re-expansion between a cluster particle S_β and the primary particle. Here, $\widehat{q}_\beta$ is given by the non-simplified expression (5.7). The multipole coefficient behaviour on S_β is taken as $0.5n(q_\beta)^n$, where q_β is obtained from (5.7) by interchanging a and $\widehat{a}$.

After these prerequisites, the truncation rules are as follows. A sufficiently large truncation order k_o is set as the bound on ν in Lamb's series (5.13) for cluster particles away from the primary particle. 'Precision' $\delta = Z_{k_o+1}(2)$ is viewed as the multipole truncation error in contact interactions between cluster particles. Now, for every pair (S_α, S_β) in the cluster with non-dimensional centre separation $\zeta_{\alpha\beta} = |\boldsymbol{x}^\beta - \boldsymbol{x}^\alpha|/a$, the first integer $L \geqslant 2$ with $[q(\zeta_{\alpha\beta})]^{L+1} Z_{L+1}(\zeta_{\alpha\beta}) < (2/\zeta_{\alpha\beta})^4 \delta$ is found (using the table interpolation for $Z_\nu(\zeta)$), and $\nu^*(\alpha,\beta) = n^*(\alpha,\beta) = L$ is used as the initial assessment. Typically, $L \ll k_o$ for well-separated cluster particles. Unexpectedly, we found that close proximity of the primary particle to one (or both) of the cluster particles S_α, S_β necessitates rather high-order multipoles (exceeding k_o) in the $S_\alpha \leftrightarrow S_\beta$ interaction, even though there is no lubrication between S_α and S_β. Such triplet effects are not captured by solution schemes with pairwise additivity. If the $S_\alpha \leftrightarrow S_{N+1}$ interaction is strong enough, so that the condition $(q_\alpha)^{\nu^*+1}/(\nu^*+1) < \delta$ is not met for the initial assessment of $\nu^*(\alpha,\beta)$, we increase $\nu^*(\alpha,\beta)$ until either this condition is satisfied, or $\nu^*(\alpha,\beta)$ reaches $1.5k_o$. Likewise, the bound $n^*(\alpha,\beta)$ is tightened for a strong $S_\beta \leftrightarrow S_{N+1}$ interaction, until $(q_\beta)^{n^*+1}/(n^*+1) < \delta$ is met, or n^* reaches $1.5k_o$. The resulting truncation bounds can be quite asymmetric, with $n^*(\alpha,\beta) \neq \nu^*(\alpha,\beta)$; however, $n^*(\alpha,\beta) = \nu^*(\beta,\alpha)$.

https://doi.org/10.1017/jfm.2014.15 Published online by Cambridge University Press

For the re-expansion between a cluster particle S_α and the primary particle S_{N+1}, the bound $\nu^*(\alpha, N+1) \geqslant 2$ is found from $0.25(\nu^*+1)(\widehat{q}_\alpha)^{\nu^*+1} < \delta$, and the bound $n^*(\alpha, N+1)$ is found from $0.25(n^*+1)(q_\alpha)^{n^*+1} < \delta$. Again, $\nu^*(N+1, \alpha) = n^*(\alpha, N+1)$ and $n^*(N+1, \alpha) = \nu^*(\alpha, N+1)$.

The bounds $\nu^*(\alpha, \beta)$ and $n^*(\alpha, \beta)$ also determine the maximum multipole order to be retained for each particle.

Appendix E. Details of the boundary-integral test

For a rigid cluster of N spheres $S_1, \ldots, S_N$ (centred at $\boldsymbol{x}^1, \ldots, \boldsymbol{x}^N$) interacting with a primary sphere S_{N+1} (centred at $\boldsymbol{x}^{N+1}$), the non-dimensional fluid velocity field outside the spheres is sought in the Power & Miranda (1987) form, as double-layer surface contributions, plus additional Stokeslet and Rotlet contributions from the particle centres to complete the range:

$$\boldsymbol{u}(\boldsymbol{y}) = \sum_{\beta=1}^{N+1} \left[2 \int_{S_\beta} \boldsymbol{q}(\boldsymbol{x}) \cdot \boldsymbol{\tau}(\boldsymbol{\xi}) \cdot \boldsymbol{n}(\boldsymbol{x}) \, \mathrm{d}S_x + \boldsymbol{F}_\beta \cdot \boldsymbol{G}(\boldsymbol{y} - \boldsymbol{x}_\beta) - \frac{\boldsymbol{T}_\beta \times (\boldsymbol{y} - \boldsymbol{x}^\beta)}{8\pi |\boldsymbol{y} - \boldsymbol{x}^\beta|^3} \right], \quad \text{(E 1)}$$

where $\boldsymbol{\xi} = \boldsymbol{x} - \boldsymbol{y}$, $\boldsymbol{n}(\boldsymbol{x})$ is the outward unit normal to S_β, and

$$\boldsymbol{\tau}(\boldsymbol{\xi}) = \frac{3\boldsymbol{\xi}\boldsymbol{\xi}\boldsymbol{\xi}}{4\pi\xi^5}, \quad \boldsymbol{G}(\boldsymbol{r}) = -\frac{1}{8\pi} \left[\frac{\boldsymbol{I}}{r} + \frac{\boldsymbol{r}\boldsymbol{r}}{r^3} \right]. \quad \text{(E 2)}$$

The hydrodynamical force $\boldsymbol{F}_\beta$ and torque $\boldsymbol{T}_\beta$ (about $\boldsymbol{x}^\beta$) acting on S_β are linked to the as-yet unknown density function $\boldsymbol{q}$:

$$\boldsymbol{F}_\beta = \int_{S_\beta} \boldsymbol{q}(\boldsymbol{x}) \, \mathrm{d}S, \quad \boldsymbol{T}_\beta = \int_{S_\beta} (\boldsymbol{x} - \boldsymbol{x}^\beta) \times \boldsymbol{q}(\boldsymbol{x}) \, \mathrm{d}S. \quad \text{(E 3)}$$

The total hydrodynamical forces and torques acting on the aggregate, and on the primary particle, are prescribed:

$$\sum_{\alpha=1}^{N} \boldsymbol{F}_\alpha = \boldsymbol{F}_h^{agg}, \quad \sum_{\alpha=1}^{N} (\boldsymbol{r}_\alpha \times \boldsymbol{F}_\alpha + \boldsymbol{T}_\alpha) = \boldsymbol{T}_h^{agg} \quad \text{(E 4)}$$

and

$$\boldsymbol{F}_{N+1} = \boldsymbol{F}_h^p, \quad \boldsymbol{T}_{N+1} = \boldsymbol{T}_h^p. \quad \text{(E 5)}$$

The standard BI equation obtained from (E 1) yields $\boldsymbol{q}(\boldsymbol{y}) = \mathrm{RHS} - [\boldsymbol{V}^{agg} + \boldsymbol{\Omega}^{agg} \times (\boldsymbol{y} - \boldsymbol{O}_g)]$ on the cluster particles and $\boldsymbol{q}(\boldsymbol{y}) = \mathrm{RHS} - [\boldsymbol{V}^p + \boldsymbol{\Omega}^p \times (\boldsymbol{y} - \boldsymbol{x}^{N+1})]$ on the primary particle, where RHS stands for the right-hand side of (E 1). Substituting these expressions into (E 3) and using (E 4)–(E 5) allows us to exclude the grand velocity 12-vector $\boldsymbol{W}$ and organize GMRES iterations for $\boldsymbol{q}(\boldsymbol{y})$ only. Upon convergence, $\boldsymbol{W}$ is obtained as well. High-order integration over spherical surfaces with unstructured triangulation (see appendix A of Zinchenko & Davis (2013)) is used to approximate the boundary integrals, after standard singularity and near-singularity subtractions.

The coordinates of all the particle centres in figure 6(*c*), used to generate table 1, are listed in table 5. All the spheres are of unit radius. The cluster centre $\boldsymbol{O}_g$ is at

https://doi.org/10.1017/jfm.2014.15 Published online by Cambridge University Press

α	1	2	3	4	5	6
x^α	0.5156708	−0.8651997	−1.2613715	0.9132592	0.6976412	−0.1717400
y^α	0.5438808	0.0419508	−1.1501821	−0.5913856	1.1557361	−0.6313505
z^α	0.8785371	−0.4785423	−2.0349062	−1.1391257	2.7740370	3.2666133

TABLE 5. Coordinates of the particle centres for the configuration in figure 6(*c*); $\alpha \leqslant 5$ for the cluster particles, and $\alpha = 6$ for the primary particle.

α	1	2	3	4	5	6
x^α	0.5443785	−0.8909842	−1.3535380	0.8571714	0.8033927	0.0395795
y^α	0.6320703	0.0387574	−1.2656076	−0.6569995	1.3854315	−0.1336521
z^α	0.1967604	−1.0634449	−2.5074255	−1.7418815	2.0313615	3.0846300

TABLE 6. Coordinates of the particle centres for the six-sphere cluster from figure 6(*d*).

the origin; the gap between the cluster particles in 'contact' is 0.0001. The prescribed forces and torques (E 4)–(E 5) are

$$\boldsymbol{F}_h^{agg} = 30\pi \boldsymbol{e}_3 - \boldsymbol{F}_{vdW}, \quad \boldsymbol{F}_h^{p} = 6\pi \boldsymbol{e}_3 + \boldsymbol{F}_{vdW}, \tag{E 6}$$

and

$$\boldsymbol{T}_h^{agg} = (-0.519210, 0.258903, 0.022742), \quad \boldsymbol{T}_h^{p} = 0, \tag{E 7}$$

where $\boldsymbol{F}_{vdW} = (-0.081700, -0.167926, 0.046471)$.

With obvious simplifications, the same test code was used to provide BI results in table 2 for an isolated six-sphere cluster from figure 6(*d*). The particle centre coordinates are listed in table 6; the cluster centre $\boldsymbol{O}_g = \boldsymbol{0}$. The total force and torque are $\boldsymbol{F}_h = 36\pi \boldsymbol{e}_3$ and $\boldsymbol{T}_h = \boldsymbol{0}$.

REFERENCES

BATCHELOR, G. K. 1972 Sedimentation in a dilute dispersion of spheres. *J. Fluid Mech.* **52**, 245–268.

BATCHELOR, G. K. & GREEN, J. T. 1972 The determination of the bulk stress in a suspension of spherical particles to order c^2. *J. Fluid Mech.* **56**, 401–427.

BINDER, C., FEICHTINGER, C., SCHMID, H.-J., THÜREY, N., PEUKERT, W. & RÜDE, U. 2006 Simulation of the hydrodynamic drag of aggregated particles. *J. Colloid Interface Sci.* **301**, 155–167.

BINDER, C., HARTIG, M. A. J. & PEUKERT, W. 2009 Structural dependent drag force and orientation prediction for small fractal aggregates. *J. Colloid Interface Sci.* **331**, 243–250.

CICHOCKI, B., FELDERHOF, B. U. & SCHMITZ, R. 1988 Hydrodynamic interactions between two spherical particles. *Physico-Chem. Hydrodyn.* **10**, 383–403.

CHOPARD, B., NGUYEN, H. & STOLL, S. 2006 A lattice Boltzmann study of the hydrodynamic properties of 3D fractal aggregates. *Maths Comput. Simul.* **72**, 103–107.

COOLEY, M. D. A. & O'NEILL, M. E. 1969 On the slow motion generated in a viscous fluid by the approach of a sphere to a plane wall or stationary sphere. *Mathematika* **16**, 37–49.

COX, R. G. & BRENNER, H. 1971 The rheology of a suspension of particles in a Newtonian fluid. *Chem. Eng. Sci.* **26**, 65–93.

DURLOFSKY, L., BRADY, J. F. & BOSSIS, G. 1987 Dynamic simulation of hydrodynamically interacting particles. *J. Fluid Mech.* **180**, 21–49.

https://doi.org/10.1017/jfm.2014.15 Published online by Cambridge University Press

EHRL, L., SOOS, M. & LATTUADA, M. 2009 Generation and geometrical analysis of dense clusters with variable fractal dimension. *J. Phys. Chem.* B **113**, 10587–10599.

FILIPPOV, A. V. 2000 Drag and torque on clusters of N arbitrary spheres at low Reynolds number. *J. Colloid Interface Sci.* **229**, 184–195.

GUCKEL, E. K. 1999 Large scale simulations of particulate systems using the PME method. PhD thesis, University of Illinois, Urbana-Champaign.

HAPPEL, J. & BRENNER, H. 1973 *Low Reynolds Number Hydrodynanmics*. Nijhoff.

HARSHE, Y. M., EHRL, L. & LATTUADA, M. 2010 Hydrodynamic properties of rigid fractal aggregates of arbitrary morphology. *J. Colloid Interface Sci.* **352**, 87–98.

HUANG, H. 1994 Fractal properties of flocs formed by fluid shear and differential settling. *Phys. Fluids* **6**, 3229–3234.

INGBER, M. S., FENG, S., GRAHAM, A. L. & BRENNER, H. 2008 The analysis of self-diffusion and migration of rough spheres in nonlinear shear flow using a traction-corrected boundary element method. *J. Fluid Mech.* **598**, 267–292.

JIANG, Q. & LOGAN, B. E. 1991 Fractal dimensions of aggregates determined from steady-state size distributions. *Environ. Sci. Technol.* **25**, 2031–2038.

JULLIEN, R., BOTET, R. & MORS, P. M. 1987 Computer simulation of cluster–cluster aggregation. *Faraday Discuss. Chem. Soc.* **83**, 125–137.

KUMAR, A. & HIGDON, J. J. L. 2011 Particle mesh Ewald Stokesian dynamics simulations for suspensions of nonspherical particles. *J. Fluid Mech.* **675**, 297–335.

LATTUADA, M., WU, H. & MORBIDELLI, M. 2003 A simple model for the structure of fractal aggregates. *J. Colloid Interface Sci.* **268**, 106–120.

LOGAN, B. E. & KILPS, J. R. 1995 Fractal dimensions of aggregates formed in different fluid mechanical environments. *Water Res.* **29**, 443–453.

LOGAN, B. E. & WILKINSON, D. B. 1990 Fractal geometry of marine snow and other biological aggregates. *Limnol. Oceanogr.* **35**, 130–136.

MEAKIN, P. 1984 Effect of cluster trajectories on cluster–cluster aggregation: a comparison of linear and Brownian trajectories in two- and three-dimensional simulations. *Phys. Rev.* A **29**, 997–999.

MEAKIN, P. 1985 Accretion processes with linear particle trajectories. *J. Colloid Interface Sci.* **105**, 240–246.

MEAKIN, P. & FAMILY, F. 1987 Structure and dynamics of reaction-limited aggregation. *Phys. Rev.* A **36**, 5498–5501.

MENG, Q. & HIGDON, J. J. L. 2008 Large scale dynamic simulation of plate-like particle suspensions. Part I: Non-Brownian simulation. *J. Rheol.* **52**, 1–36.

MO, G. & SANGANI, A. S. 1994 A method for computing Stokes flow interactions among spherical objects and its application to suspensions of drops and porous particles. *Phys. Fluids* **6**, 1637–1652.

O'NEILL, M. E. & MAJUMDAR, S. R. 1970 Asymmetrical slow viscous fluid motions caused by the translation or rotation of two spheres. Part II: Asymptotic forms of the solutions when the minimum clearance between the spheres approaches zero. *Z. Angew. Math. Phys.* **21**, 180–189.

POWER, H. & MIRANDA, G. 1987 Second kind integral equation formulation of Stokes flow past a particle of arbitrary shape. *SIAM J. Appl. Maths* **47**, 689–698.

SANGANI, A. S. & ACRIVOS, A. 1982 Slow flow through a periodic array of spheres. *Int. J. Multiphase Flow* **8**, 343–360.

SANGANI, A. S. & MO, G. 1994 Inclusion of lubrication forces in dynamic simulations. *Phys. Fluids* **6**, 1653–1662.

SCHAEFER, D. W. 1989 Polymers, fractals and ceramic materials. *Science* **243**, 1023–1027.

SCHMITZ, R. & FELDERHOF, B. U. 1982 Creeping flow about a spherical particle. *Physica* **113A**, 90–102.

SIEROU, A. & BRADY, J. F. 2001 Accelerated Stokesian dynamics simulations. *J. Fluid Mech.* **448**, 115–146.

SUTHERLAND, D. N. 1966 Comments on Vold's simulation of floc formation. *J. Colloid Interface Sci.* **22**, 300–302.

THOUY, R. & JULLIEN, R. 1996 Structure factors for fractal aggregates built off-lattice with tunable fractal dimension. *J. Phys.* I *(Paris)* **6**, 1365–1376.

https://doi.org/10.1017/jfm.2014.15 Published online by Cambridge University Press

TORRES, F. E., RUSSEL, W. B. & SCHOWALTER, W. R. 1991*a* Floc structure and growth kinetics for rapid shear coagulation of polystyrene colloids. *J. Colloid Interface Sci.* **142**, 554–574.

TORRES, F. E., RUSSEL, W. B. & SCHOWALTER, W. R. 1991*b* Simulations of coagulation in viscous flows. *J. Colloid Interface Sci.* **145**, 51–73.

VANNI, M. 2000 Creeping flow over spherical permeable aggregates. *Chem. Engng Sci.* **55**, 685–698.

VERWEY, E. J. W. & OVERBEEK, J. TH. G. 1948 *Theory of the Stability of Lyophobic Colloids*. Elsevier.

ZINCHENKO, A. Z. 1994 An efficient algorithm for calculating multiparticle thermal interaction in a concentrated dispersion of spheres. *J. Comput. Phys.* **111**, 120–135.

ZINCHENKO, A. Z. 1998 Effective conductivity of loaded granular materials by numerical simulation. *Phil. Trans. R. Soc. Lond.* A **356**, 2953–2998.

ZINCHENKO, A. Z. & DAVIS, R. H. 2000 An efficient algorithm for hydrodynamical interaction of many deformable drops. *J. Comput. Phys.* **157**, 539–587.

ZINCHENKO, A. Z. & DAVIS, R. H. 2002 Shear flow of highly concentrated emulsions of deformable drops by numerical simulations. *J. Fluid Mech.* **455**, 21–62.

ZINCHENKO, A. Z. & DAVIS, R. H. 2008 Algorithm for direct numerical simulation of emulsion flow through a granular material. *J. Comput. Phys.* **227**, 7841–7888.

ZINCHENKO, A. Z. & DAVIS, R. H. 2013 Emulsion flow through a packed bed with multiple drop breakup. *J. Fluid Mech.* **725**, 611–663.

ZINCHENKO, A. Z., ROTHER, M. A. & DAVIS, R. H. 2011 Gravity-induced collisions of spherical drops covered with compressible surfactant. *J. Fluid Mech.* **667**, 369–402.

https://doi.org/10.1017/jfm.2014.15 Published online by Cambridge University Press